Advanced Steel Construction – Vol. 21 No. 1 (2025) 1–20
DOI:10.18057/IJASC.2025.21.1.1

WIND RESISTANCE PERFORMANCE AND REINFORCEMENT MEASURES OF STANDING SEAM METAL ROOFS BASED ON WIND TUNNEL TESTS

Wen-Bing Han [1], Jing-Zhen Chen [2, *], Bo Yang [1], Hua-Chang Liu [2], Kai-Fang Lv [2], Chu-Huang Huang [2] and Mohamed Elchalakani [3]

[1] School of Civil Engineering, Chongqing University, Shapingba District, Chongqing 400045, China
[2] China Construction Fourth Engineering Division Corp., LTD, Xiamen 361000, China
[3] Department of Civil, Environmental and Mining Engineering, University of Western Australia, Crawley, WA 6009, Australia
** (Corresponding author: E-mail: 1578339351@qq.com)*

ABSTRACT

As an important building envelope structure, metal roofs have been widely used in various large-scale buildings because of their unique advantages such as beautiful shape, lightweight nature, flexibility, and exceptional strength. However, there are still some gaps in the existing research on the wind resistance performance of metal roof systems, which poses a serious threat to life and property. To address this gap, this paper conducted wind tunnel tests of long-span standing seam metal roofs. The basic wind pressure of 0.95 kN/m^2, which is once every 100 years. The wind-induced response of the metal roofs under varying wind speeds and wind directions was simulated by the wind tunnel tests, which involved the measurement and analysis of the load distribution characteristics, equivalent wind loads, and wind vibration coefficients. The experimental results were used to determine the design wind load for the metal roofing structure and to conduct the wind vibration calculations. The results indicated that in regions experiencing high negative wind pressure, the results obtained from extreme value analysis marginally exceeded those obtained through the peak factor method. The stress characteristics and instability modes of metal roofs in strong wind environments were summarized, and the factors affecting the wind resistance performance of metal roofs were analyzed. The reinforcement measures for wind resistance design of metal roofs were proposed, it serves as a theoretical guide and scientific foundation for the future development of similar metal roof structures.

ARTICLE HISTORY

Received:	12 June 2024
Revised:	17 December 2024
Accepted:	20 December 2024

KEYWORDS

Large span metal roofs;
Wind tunnel tests;
Wind resistance performance;
Finite element analysis;
Reinforcement measures

1. Introduction

The metal roof serves as a crucial exterior maintenance structure boasting notable advantages of beautiful appearance, lightweight construction, corrosive resistance, and facilitation of installation [1-3]. Its significance extends beyond mere aesthetics, encompassing essential functions like waterproofing, thermal insulation, and decorative purposes within building structures [4,5]. Generally, metal roofing is exposed to a variety of complex loads, including alternating wind loads, temperature variations, and precipitation [6-9]. It is not uncommon for metal roofing to be damaged by wind loads, safety concerns such as metal roofing flying off and collapsing have also attracted considerable attention [10-13]. Therefore, it is imperative to investigate the dynamic response of metal roofs to wind-induced vibrations, and it will also promote the application and development of metal roofs in regions susceptible to typhoons [14,15].

With the increase in extreme weather events, the wind resistance of metal roof structures has gradually attracted attention. Numerous scholars have studied the mechanical properties of metal roofing under wind loads by experiments and numerical analysis [16,17]. Baskaran et al. [18] conducted wind tunnel tests to examine three prevalent standing seam metal roofing structures and proposed a simplified design method for assessing the wind-bearing capacity of metal roofing. Schroter et al. [19] predominantly explored the key factors affecting the wind-bearing capacity of roof panels through static testing. Xu et al. [20] utilized a combination of experimental trials and numerical simulations. The results indicated that the key parameters influencing the wind-bearing capacity included the bite-bearing capacity of lock joints and fixed supports within roof panels. Farquhar et al. [21] conducted small-scale uniform uplift and wind tunnel tests on a standing seam roof model. A pressure coefficient capable of correlating uniform uplift failure pressures with the actual wind pressures was proposed. Compared with the traditional sliding supports, the wind load capacity and failure mode of the metal roof system using the novel sliding support with high tensile and wind resistance are improved [22]. Sinno et al. [23] also studied the wind resistance of standing seam roofing panels through experiments, it is indicated that the pivotal determinants affecting wind resistance capacity are the connections between individual roof panels and the supports linking these panels. Li et al. [24] investigated the influence of various parameters (e.g., purlin spacing, roof slab thickness, and slab width) on the wind uplift resistance of standing seam roofing slabs through theoretical analysis. Based on an effective method to evaluate the wind resistance behavior of standing seam metal systems, the wind-induced structural response of the system was investigated experimentally and numerically, including the displacement of metal plates, stress, and the reaction force of clips [25,26].

Numerous investigations have been conducted to evaluate the wind-bearing capacity of metal roofing under dynamic loading conditions. Simiu et al. [27], Petrov et al. [28], and Suresh et al. [29] specifically investigated the impact of various wind loads on the fatigue performance of metal roofing, and a methodology for calculating wind-induced fatigue damage was proposed. Additionally, Myuran et al. [30,31] focused on the mechanical properties of metal roof panels subjected to cyclic wind loads through experimental tests and proposed a new anti-fatigue design method for metal roof panels. Given the wind vibration vulnerability of standing seam metal roof systems, the failure process of roof systems under wind load was analyzed considering fatigue damage, and the vulnerability of different types of roof systems was compared [32,33]. Habte and Homles et al. [34,35] conducted dynamic loading tests on full-size standing seam metal roof panels and discussed the effects of roof panel type and specimen design on wind-bearing capacity. Luo et al. [36] explored the dynamic response of large-span metal roofs under repeated wind loads through dynamic loading tests, indicating that the new type of metal roofing structure exhibits favorable seismic performance. The latest application of Computational Fluid Dynamics technology (CFD) in wind field analysis and its comparison with traditional wind tunnel experiments are discussed, and it is shown that the use of CFD provides good calculation accuracy [37]. The application and future development of CFD in wind resistance design of metal roofing in high-rise buildings are summarized [38,39]. Aiming at the design of metal roofing, Baskaran et al. [40,41] carried out a series of fatigue tests. The wind resistance performance of various roof structures under repeated wind loads and the bolted joint performance is evaluated. A new method for calculating the wind-bearing capacity of lightweight metal roofing is proposed.

Currently, significant advancements have been made in the wind resistance of metal roofs, encompassing areas such as wind pressure distribution, roof shape optimization, dynamic response, aeroelastic performance, support connections, and purlin fastening systems, as well as the durability and corrosion resistance of roofing materials [1,16,26]. Moreover, wind tunnel testing remains fundamental for understanding wind loads and optimizing roof design, with the development of more accurate scale models to improve the simulation of complex roof geometries [2,9,15,32]. Combining the wind tunnel test results with the structural response models, the wind resistance of the roofs under wind loads is comprehensively analyzed. Computational Fluid Dynamics (CFD) has become a critical method for studying wind loads, with growing emphasis on the interaction between wind and structures, considering factors such as vortex shedding, flow separation, and the resulting pressure variations [37,39]. This is especially crucial for understanding the aeroelastic behavior of metal roofs and for designing systems that reduce wind-induced vibrations or instabilities. The combined advancements in wind tunnel testing and CFD have exhibited a profound impact on the design and optimization of metal roofs. These developments contribute to the updating of international design standards and codes, ensuring that they more accurately reflect wind load predictions based on advanced testing and simulation methods [10,25,37].

Compared with the traditional roof system, the standing seam metal roof system can effectively release temperature-induced stress, in which the rolling edge of the adjacent roof plate is occluding with the support riser through the electric locking machine, and then the support is bolted to the purlin [17,21,42]. Extensive investigations have been conducted on the wind-resistant design of metal roofing, including both experimental tests and theoretical analysis. Various wind exposure test methods (e.g., ASTM E1592 [43], ANSI/ FM 4474 [44], and UL 1897 [45]) for standing seam roofing systems were proposed. However, the existing design specifications lack comprehensive determinations for the design wind loads of standing seam roofing, primarily due to the complexity and diversity of metal roofing loads. Based on the metal roof project of the Xiamen International Expo Center (XIEC), this paper focuses on the wind resistance performance of large-span metal roofs under wind loads by the wind tunnel tests, which advances the application and development of metal roofing within large-span building structures.

2. Project overview

The project is situated southwest of the intersection of Binhai East Avenue and Xiang 'an Tunnel, Xiamen City, which is the coastal core area of Xiamen East Sports Exhibition New City. The conference center project covers a total area of 107439318 m^2, a total construction area of 231100 m^2, an above-ground construction area of 169000 m^2, a building height of 68.55 m, featuring its most expansive span at 81 m, belonging to a class of high-rise buildings. Additionally, the design mandates consideration of a basic wind pressure occurrence once in a century, adding complexity to the overall roof design. The installation process poses challenges in ensuring adherence to the design scheme for the overall linear shape, while simultaneously meeting the stringent quality requirements for wind resistance and leak prevention. The overall layout of the project is illustrated in **Fig. 1**, including the conference center, exhibition hall (3W), land-side exhibition hall (2.4W), sea-side exhibition hall (2.4W), login hall, corridor, belvedere and warehouse.

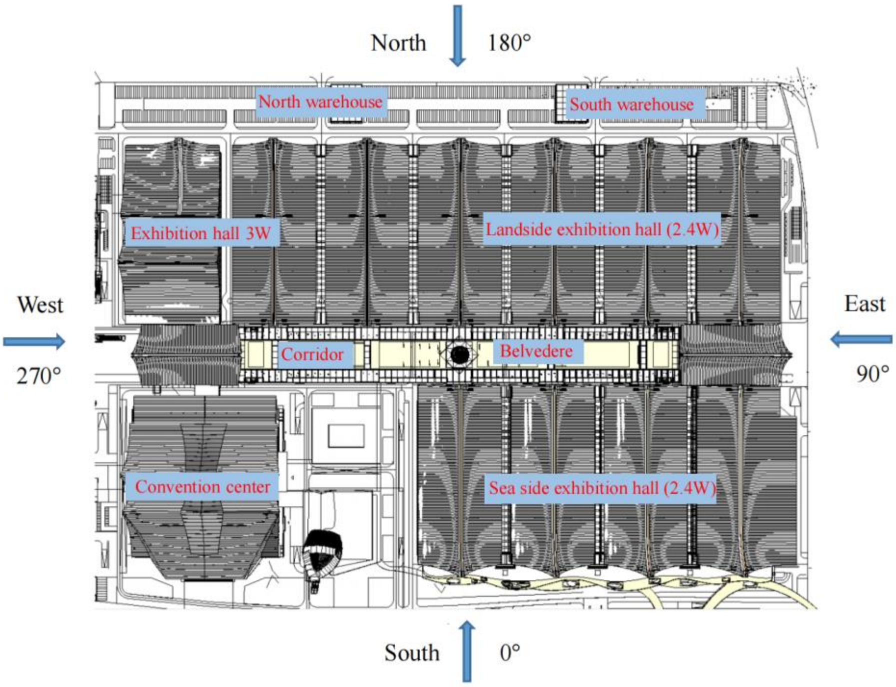

Fig. 1 Overall layout of Xiamen International Expo Center

The model of the conference center is depicted in **Fig. 2**. The primary framework comprises steel frames (reinforced concrete columns) and steel trusses. The warehouse adopts a portal frame and steel truss structure, while the flooring incorporates a combination of composite steel plates and concrete slabs. The roofing systems include a double metal roofing system, a single daylighting roofing system, a drainage gutter system, an eaves gutter system, and connections featuring aluminum plates for eaves and gutters. The roofing system structure in this project is up to 9 layers, the overall height of the structural layer ranging from approximately 850 mm to 1000 mm. The roofing shape ascends 31 meters above the highest structural layer, and the cornice roof extends as far as 6 m beyond the lower facade. Notably, the maximum curvature of the roofing surface exceeds 1/22. The formation of the curved surface primarily relies on the roofing steel structure line, roofing purlin line, ridge eaves line, and the surface layer comprised of metal plates, aluminum plates, and honeycomb plates.

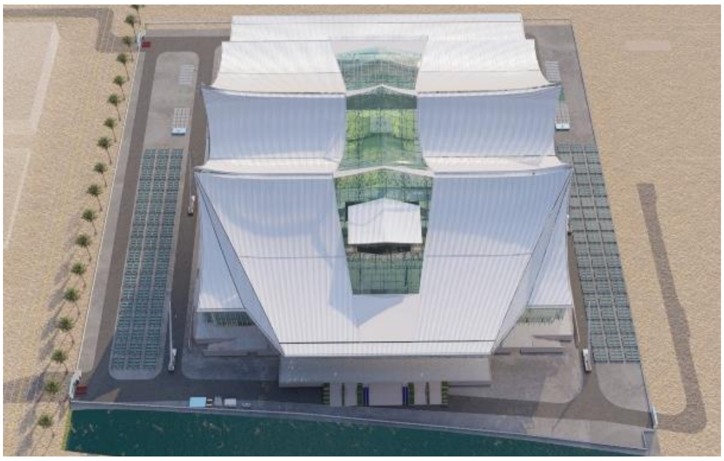

Fig. 2 Global view of the conference center

3. Wind tunnel test

3.1. Model and measuring point arrangement

Due to the intricate design of the conference center, the existing specifications lack the corresponding body shape coefficient and wind vibration coefficient for this distinctive building structure. It is necessary to conduct wind tunnel tests and wind vibration calculations for the metal roofing of the conference center to ensure the safety, cost-effectiveness, and soundness of the structural design, as well as to fulfill the design criteria for wind-resistant uplift. To simulate the wind loads of long-span metal roofs under different wind speeds, a wind tunnel test platform was constructed, which can simulate the airflow conditions and the stress distributions experienced by the metal roofing under different wind speeds.

The wind tunnel test model of metal roofing is a rigid model, which is made of glass fiber reinforced plastic, Plexiglas, and ABS plastic according to the geometric similarity, and certain components were produced using 3D printing technology. The scale of the model is 1:220, as shown in **Fig. 3**. The test is carried out in the CGB-2 wind tunnel laboratory (test section 8 m×5 m). The maximum plugging area of the model is about 1.25 m^2, with a corresponding maximum plugging ratio of 3.2%, which met the requirement not greater than 5% in JGJ/T 338-2014 (Standard for wind tunnel test of buildings and structures) [46]. The dimensionless parameters such as the wind pressure coefficient obtained from the wind tunnel test can be directly applied to the design of building structures.

(a) Front view (b) Back view

Fig. 3 Wind tunnel test model

Table 1

Summary of measuring points

Number	Object	Total number of points	Description
1	Conference center	1034	
2	Exhibition hall of 3W	544	
3	Landside exhibition hall of 2.4W	466	3 exhibition halls： L1, L2, L3
4	Seaside exhibition hall of 2.4W	478	3 exhibition halls： H1, H2, H3
5	Entrance hall	402	
6	Belvedere	16	
7	Corridor	84	
8	North warehouse	98	2 warehouses： B1, B2
Total		5108	

Table 1 summarizes the all measuring points layout. This paper focuses on elucidating the arrangement of measuring points within the conference center. A total of 1034 measuring points in the conference center including the upper surface of the upper metal roofing (A:56, B:43, C43, D:51, E:51, F:49, G:49, H:38, J:38, K:36), upper surface of lower metal roofing (M:18, N:16, P:56), lower surface of upper metal roofing (AX: 54, KX: 16), and lower surface of lower metal roofing (AX:54, KX:16, PX:56).

3.2. Experimental program and test method

3.2.1. Wind tunnel tests and equipment

The experiment was conducted within the confines of the CGB-2 boundary layer wind tunnel laboratory. The enclosed test section spans a length of 34 meters, with a cross-section measuring 8 m in width and 5 m in height. The maximum wind speeds up to 35 m/s, and the reference wind speed of the testing flow field is measured and monitored by micro pressure gauges. A Dandy 4-channel hot wire anemometer system is used to simulate the atmospheric boundary layer in the wind field. The wind pressure measurement process involved an electronic scanning valve, a data acquisition board, and a proprietary signal acquisition and data processing software, constituting a comprehensive wind pressure measurement and recording system.

3.2.2. Wind field simulation

Based on the surrounding topography and geomorphic characteristics, the geomorphic roughness index (α) is determined as 0.12. The basic wind pressure once in 100 years is 0.95 kN/m^2, which is equivalent to the wind speed (U_0) of 38.99 m/s at a height of 10 m above the ground. Wind speed at different heights above the ground is described using Eq. (1).

$$U_z = U_0 \left(Z / Z_0 \right)^{\alpha} \tag{1}$$

Where U_0 is the average wind speed at the height of 10 m above the ground, the 50-year recurrence period, U_z is the average wind speed at the height of Z from the ground.

During the wind tunnel test, the wind speed profile is simulated and verified by the multifunctional simulation device at the wind entrance and the rough element situated at the bottom wall of the wind tunnel. The measured wind speed curves at different heights away from the bottom wall of the wind tunnel are shown in **Fig. 4 (a)**, and are compared with the theoretical curves calculated by Eq. (1). It is found that the relative error is minimal, which indicates that the wind tunnel simulation is in good agreement with test results.

In the atmospheric boundary, the airflow comprises numerous eddies of varying intensity, and turbulence is a key parameter to characterize the intensity of eddies. Turbulence decreases with the increase of the altitude above the ground, which is related to the average wind speed, time interval, and ground roughness. According to the GB 50009-2012 (Load code for the design of building structures) [47], the variation of turbulence with height is described by Eq. (2).

$$I_u = I_{10} \left(\frac{Z}{10} \right)^{-\alpha} \tag{2}$$

Where Z is the height from the ground, I_{10} is 10 m high nominal turbulence. The turbulence simulated by the wind tunnel is shown in **Fig. 4 (b)**, it is found that the simulation results are close to the theoretical calculated value of Eq. (2). The accurate simulation of the wind tunnel flow field provides a significant guarantee for the reliability of average wind pressure and fluctuating wind pressure measurement.

To verify the accuracy of the scale model and wind tunnel settings, the correctness of the scale model was confirmed by ensuring geometric similarity, Reynolds number similarity, and dynamic similarity. The accuracy of the wind tunnel settings was validated through flow field testing, environmental monitoring, and boundary effect control. Additionally, the reliability of the experiment was further validated by comparing it with theoretical predictions, conducting repeated tests, and cross-checking with field tests.

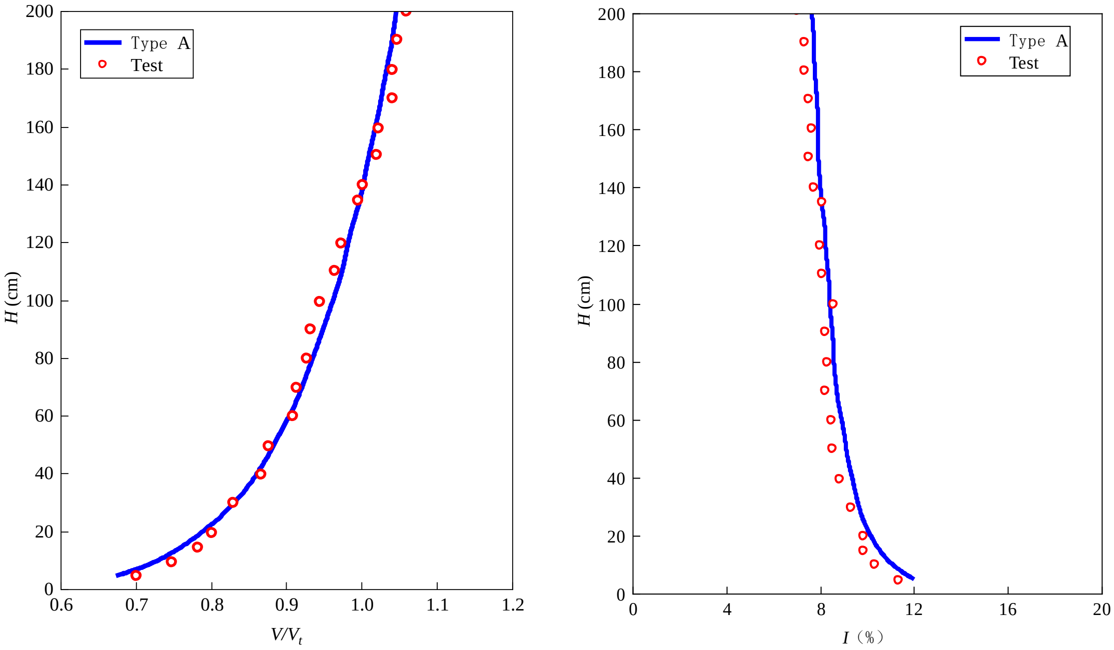

(a) Wind speed profile (b) Turbulence intensity profile

Fig. 4 Class A atmospheric boundary characteristics simulated by wind tunnel test

3.2.3. Test method

Following the completion of the atmospheric boundary layer simulation in the wind tunnel, the model is installed on the turntable in the test section of the wind tunnel. During the wind tunnel test, each wind direction angle constitutes a distinct load condition, with a 15° interval for wind direction changes. The wind direction angles from 0° to 360°, including 24 distinct load conditions. As shown in **Fig. 1**, the wind direction angle of 0° and the rotation center are defined, and the wind direction of each load condition is increased counterclockwise for one cycle around the rotation center.

3.3. Analysis of the test results

3.3.1. Wind pressure coefficient

While both dynamic wind pressure and static wind pressure wind tunnel tests employ rigid models, the testing methodologies and contents differ significantly. Dynamic wind pressure test uses an electronic scanning valve and a data acquisition system to capture the pressure spectrum at each measuring point in a period in the wind field simulating turbulence, to obtain the wind pressure coefficient. According to the international test standards, the dynamic wind pressure sampling time should be equivalent to 10 minutes, and the data samples collected must be enough to obtain real statistical data. The wind pressure coefficient of each measuring point is determined in line with JGJ/T 338-2014 [46], as shown in Eq. (3).

$$C_{pi}=\frac{p_i-p_\infty}{0.5\rho v_\infty^2} \tag{3}$$

Where the C_{pi} represents the wind pressure coefficient of a specific measuring point i on the building surface; P_i is the wind pressure value of measuring point i; P_∞ is the static pressure of the reference point; V_∞ is the wind speed at the reference point. For this test, V_∞= 12.4 m/s, and the reference point is situated at the model height of 0.6 m, corresponding to the real height of 132 m. According to the similarity principle, the dimensionless parameters of the model are consistent with the real structure, so the C_{pi} on the model is the average wind pressure coefficient of the corresponding point on the real structure.

3.3.2. Mean wind pressure

For this wind tunnel test, the geomorphic index (α) is 0.12, the height of the wind speed reference point H is 132 m, and the basic wind pressure (w_0) is 0.95 kN/m^2 once every 100 years. The reference wind pressure can be calculated using Eq. (4a). Where z_i represents the body shape coefficient of any point, and the local body shape coefficient corresponding to each measuring point (μ_{zi}) is obtained by Eq. (4b).

$$W_r=\mu_{zr}w_0=1.284\times\left(\frac{132}{10}\right)^{0.24}\times0.95=2.266\left(\mathrm{kN/m^2}\right) \tag{4a}$$

$$\mu_{zi}=\left(\frac{132}{z_i}\right)^{0.24} \tag{4b}$$

In wind resistance design, it is imperative to account for the maximum wind pressure under each wind direction while considering the predominant local wind direction. For the awning test area, both the upper and lower surfaces experience simultaneous wind loading, and the wind pressure difference should be considered in the design. The wind pressure difference is defined as the wind pressure on the upper surface minus that on the lower surface, and the positive and negative signs of the wind pressure are the same as that of the upper surface. The net wind pressure coefficient (C_{pms}) of each measurement point can be calculated using Eq. (5). Where C_{pu} and C_{pl} denote the wind pressure coefficient of the upper and lower surface, respectively.

$$C_{pms}=\sqrt{\sum_{k-1}^{N}\left(C_{pu}-C_{pl}\right)^2\Big/\left(N-1\right)} \tag{5}$$

For the awning test area, the upper and lower surfaces have been superimposed, and the numbering rule of the test points after combined is to change the number to lowercase to show the difference, such as the test points S9 and SX9 are denoted as s9 after superimposed. Taking the metal roof of the conference center as an example, the wind pressure coefficient and body shape coefficient of each measuring point under various wind direction angles are analyzed and calculated, the results are listed in **Table 2**.

During periods of heightened average wind pressure on the roofing, the wind direction angles associated with positive and negative wind pressure for the same measuring point differ. For the upper surface of the roof, the average maximum positive wind pressure reaches 1.00 kN/m², accompanied by a corresponding maximum body shape coefficient of 0.62, at that time the wind direction angle is 315°. At a wind angle of 240°, the maximum negative wind pressure (-4.80 kN/m²) is achieved, and the body shape coefficient is -2.85. For the whole conference center, the point of the west facade ridge curtain wall (O22) experiences the maximum positive wind pressure of 1.68 kN/m², with a shape coefficient of 0.92 and a wind direction of 285°. The maximum negative wind pressure (-4.84 kN/m²) occurs at the measuring point (P13) on the upper surface of the lower roof, the corresponding body shape coefficient is -3.05, and the wind direction is 225°. As shown in **Fig. 5**, the distribution of average wind pressure under different wind pressure coefficients and body shape coefficients is shown. It can be found that with the increasing wind pressure coefficient and body shape coefficient, the positive and negative average wind pressure increases linearly, and its increasing law conforms to a plane.

Table 2

Summary of the test results with average wind pressure

Measure distribution		Positive wind pressure				Negative wind pressure			
Location	Point ID	Wind pressure coefficient (C_{pi})	Average wind pressure (kN/m²)	Shape coefficient (Zi)	Wind direction (°)	Wind pressure coefficient (C_{pi})	Average wind pressure (kN/m²)	Shape coefficient (Zi)	Wind direction (°)
The upper roof covers the upper surface	A1	0.29	0.66	0.41	285	-1.52	-3.43	-2.15	45
	B4	0.44	1.00	0.62	315	-1.15	-2.61	-1.66	285
	C10	0.34	0.77	0.47	330	-1.66	-3.77	-2.29	60
	D51	0.24	0.54	0.29	300	-1.03	-2.32	-1.25	300
	E47	0.11	0.24	0.14	285	-1.17	-2.64	-1.42	75
	F19	0.43	0.97	0.51	345	-1.20	-2.73	-1.41	225
	G9	0.34	0.77	0.42	30	-1.54	-3.50	-1.81	30
	H2	0.37	0.85	0.46	195	-1.55	-3.50	-2.07	240
	J1	0.32	0.73	0.39	165	-1.22	-2.75	-1.49	30
	K36	0.06	0.14	0.08	165	-2.12	-4.80	-2.85	240
The lower roof covers the upper surface	M3	0.25	0.56	0.35	210	-1.27	-2.89	-1.79	270
	N10	0.21	0.49	0.30	165	-0.91	-2.07	-1.29	270
	P13	0.15	0.35	0.22	165	-2.13	-4.84	-3.05	225
The lower surface of the roof	AX41	0.61	1.37	0.91	330	-0.56	-1.27	-0.85	300
	KX10	0.24	0.54	0.33	165	-1.22	-2.77	-1.67	225
	PX1	0.45	1.01	0.65	255	-0.67	-1.53	-0.99	210
Belvedere	Z1	0.79	1.80	1.05	285	-1.72	-3.91	-2.23	30
West elevation ridge curtain wall	Q22	0.74	1.68	0.92	285	-1.40	-3.18	-1.75	210
	S17	0.68	1.55	0.87	285	-0.76	-1.72	-1.08	165
East elevation ridge curtain wall	R22	0.71	1.62	0.89	60	-1.31	-2.98	-1.92	315
	T17	0.64	1.46	0.82	60	-0.98	-2.21	-1.91	300
South facade curtain wall	U23	0.72	1.63	1.15	60	-0.96	-2.17	-1.88	15
North facade curtain wall	V23	0.51	1.15	0.82	225	-0.49	-1.12	-0.97	210
West side canopy	W5	0.55	1.24	0.85	285	-0.76	-1.71	-1.17	165
East side canopy	Y7	0.56	1.26	0.86	75	-0.91	-2.06	-1.41	300

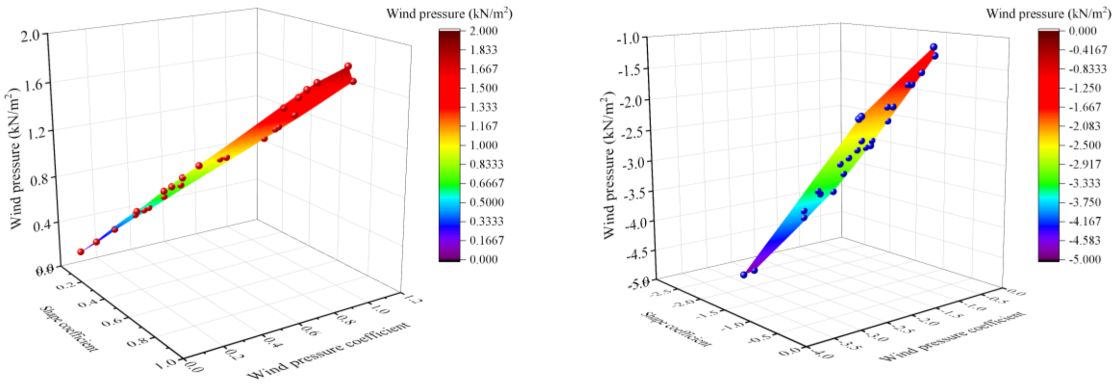

(a) Positive wind pressure

(b) Negative wind pressure

Fig. 5 Distribution of average wind pressure

3.3.3. Isogram of body shape coefficient

Fig. 6 takes the body shape coefficient of the upper surface of the roof of the conference center as an example and shows the contour distribution diagram when the shape coefficient reaches the ultimate values under positive and negative wind pressure. When the wind direction is 315°, the contour lines of the body shape coefficient concentrate on the roof surface, depicting predominantly negative wind pressure across most areas, as shown in **Fig. 6 (a)**. Notably, within the southern portion of the conference center, there exist more areas experiencing positive wind pressure, resulting in relatively sparse contour lines. As shown in **Fig. 6 (c)**, when the wind direction is 210°, the distribution of contour lines for the shape coefficient on the upper roof surface reveals three primary areas. The northern and southern sides of the roof primarily encounter positive wind pressure zones, whereas the central part predominantly experiences negative wind pressure, significantly influenced by variations in wind direction angles.

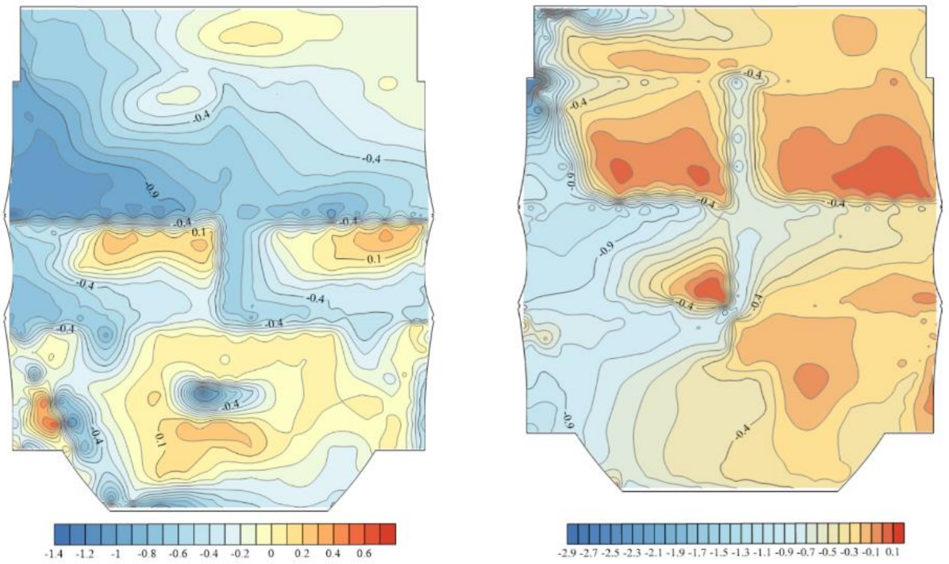

(a) 315°（μ=0.62） (b) 240°（μ=-4.80）

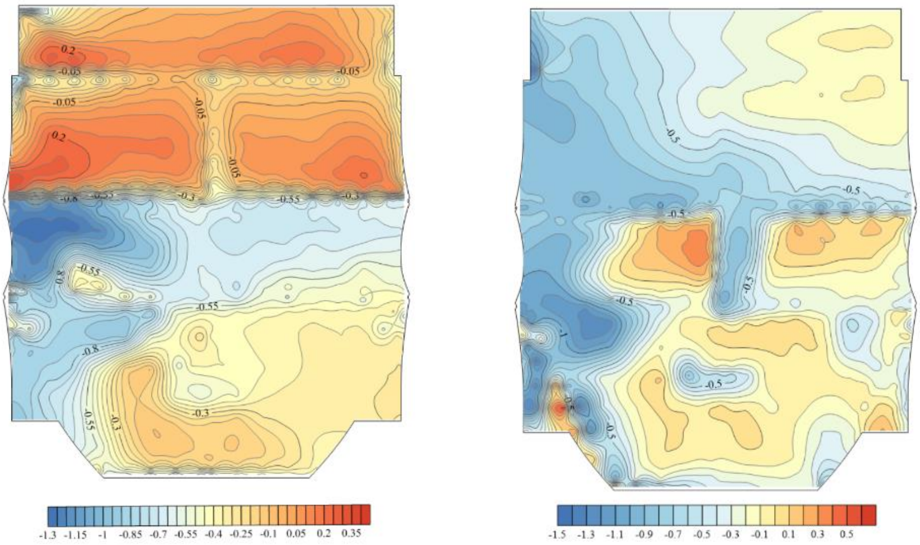

(c) 210°（μ=0.08） (d) 300°（μ=-2.23）

Fig. 6 Distribution of body shape coefficient at different wind direction angles

4. Standard wind load of the enclosure structure

4.1. Comparison of calculation methods

At present, there are two main methods to calculate the standard wind load of the metal roof envelope structure, including the peak factor method (PFM) and the extreme value analysis method (EAM). Compared to other methods, the PFM and EAM have unique advantages in the wind resistance design of metal roofs. Utilizing statistical analysis and empirical formulas, these methods are highly effective in addressing extreme fluctuations, uneven distribution, and complex local effects of wind loads, making them widely adopted in engineering practice. By providing a more accurate assessment of extreme wind loads, they help ensure the safety and stability of metal roofs under severe wind conditions. In contrast, traditional formula-based methods and standard approaches typically fail to fully capture extreme wind loads and the dynamic response of the structure. As a result, they are not suitable for all types of structures, particularly those that require consideration of extreme wind speeds and dynamic effects. The following two methods are used for analysis and calculation.

4.1.1. Peak factor method (PFM)

Fluctuating wind pressure is an important factor for the design of curtain walls, roof plates, and connectors, so it is necessary to analyze the wind pressure coefficient and wind load at each point after considering the wind pressure fluctuation. According to the probability and statistical theory, and ensuring a 99.98% reliability rate, the maximum positive and negative values of the fluctuating wind pressure coefficient (C_p) of the metal roof of the conference center can be determined using the Eqs. (6).

$$C_{P\max} = \overline{C}_{pi} + 3.5C_{pi} \tag{6a}$$

$$C_{P\min} = \overline{C}_{pi} - 3.5C_{pi} \tag{6b}$$

As a common enclosed building structure, the internal pressure of the conference center itself should be considered when calculating the standard wind load. Corresponding to the positive and negative conditions of the outer surface, the local body shape coefficient of the internal pressure of the building is -0.2 and 0.2, respectively. Therefore, the design wind load value of the envelope structure should be superimposed on the wind pressure of the outer surface and the inner surface, which can be calculated using Eqs. (7).

$$W_i^{\max} = (\overline{C}_{pi} + 3.5C_{pi})W_r + 0.2\beta_{gz}\mu_z W_0 \tag{7a}$$

$$W_i^{\min} = (\overline{C}_{pi} - 3.5C_{pi})W_r - 0.2\beta_{gz}\mu_z W_0 \tag{7b}$$

Where the W_i is designed wind load of the envelope structure, W_r is the wind pressure value of the outer surface obtained by the wind tunnel test, and the basic wind pressure once in 100 years is W_0. The wind vibration coefficient is defined as $\beta_{gz} = 1 + 2gI_{10}(z/10)^{-\alpha}$, and 0.12 is taken for class A landform I_{10}, μ_z is the local body shape coefficient corresponding to each measuring point

4.1.2. Extreme value analysis method (EAM)

The Gumbel fitting method assumes that the ultimate value of the wind pressure coefficient conforms to the Gumbel distribution, that is, the extreme value type I distribution, and the distribution function is shown in Eq. (8). Where μ and β are the positional and scale parameters of Gumbel distribution, respectively.

$$F(x) = \exp[(-\exp(-\frac{x-\mu}{\beta})] \tag{8}$$

The time history of the wind pressure coefficient is divided into *n* subsamples of equal length. Within each subsample, the maximum and minimum values are extracted and subsequently arranged in ascending order. Lieblein BLUE (Best Linear Unbiased Estimator) method was used to determine the distribution coefficients μ and β. The average Gumbel distribution is taken to estimate the extreme value wind pressure, as shown in Eq. (9).

$$E(x) = \mu + \gamma\beta \tag{9}$$

Where γ=0.5772 signifies the Euler-Mascheroni constant. The BLUE algorithm is widely used in wind speed and extreme value wind pressure statistics. Notably, the BLUE algorithm holds prominence in statistical analyses of wind speed and extreme value wind pressure, garnering endorsement from both the ASCE specifications. The wind load value of the outer surface obtained through the EAM also needs to consider the correction of the internal pressure. This correctional approach aligns with the methodology delineated in Eq. (7).

4.1.3. Comparison of the calculated results

Two typical positions B40 (the middle position) and E33 (the windward angle area) of L1 in the exhibition hall (2.4W) under the wind angle of 135° were taken respectively to compare and analyze the rationality of the two calculation methods, as shown in **Fig. 7**. It is observed that the two methods exhibit close agreement within the Gaussian distribution region. For the non-Gaussian distribution region, the EAM shows more reasonable results. The wind pressure curves of the two measuring points are enveloped in the range of positive and negative wind pressure curves obtained by EAM. However, for E33 in the corner region, the upper limit of the wind pressure line calculated by the PFM significantly deviates from the actual wind pressure time history curves.

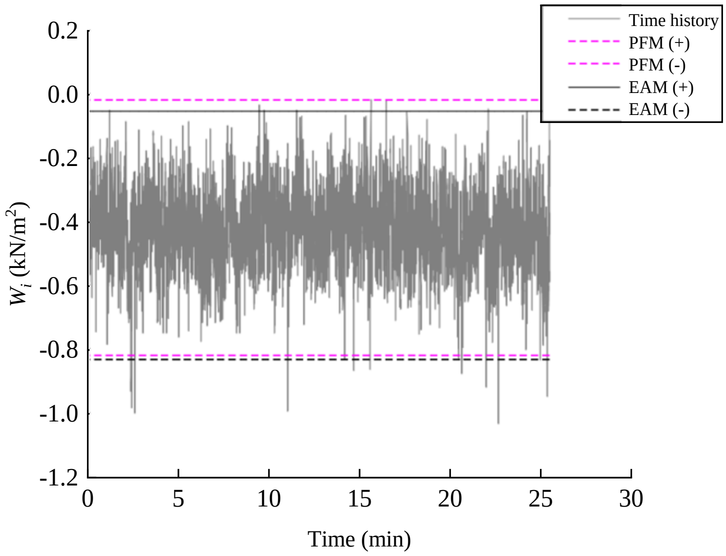

(a) B40

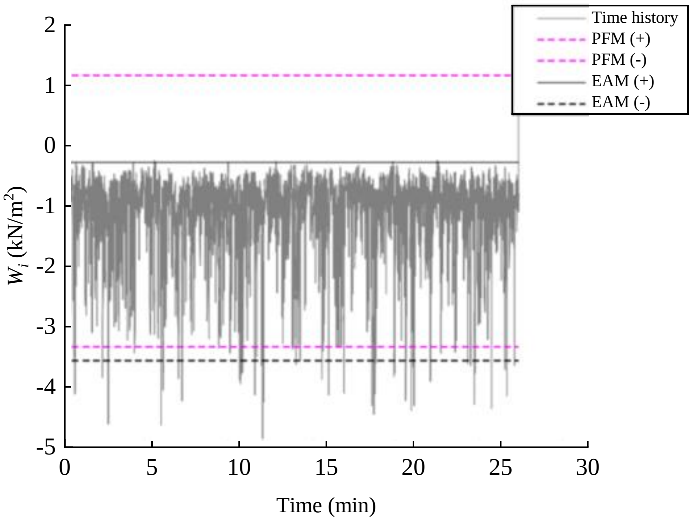

(b) E33

Fig. 7 Comparison of calculation results of two statistical methods

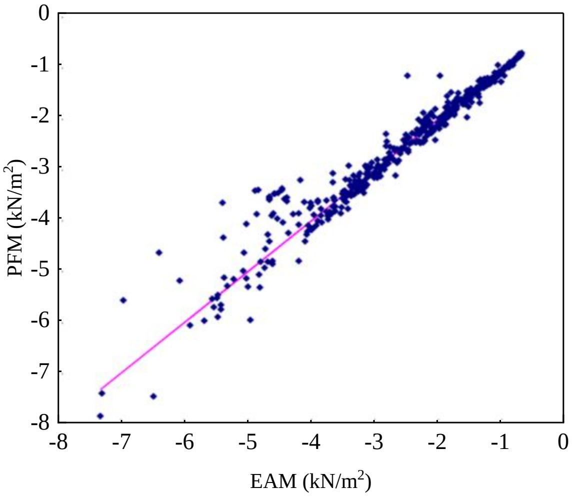

Fig. 8 Comparison of extreme wind pressure

Fig. 8 depicts the comparison of the extreme negative wind pressure in the design wind load of the L1 enclosure structure of the exhibition hall (2.4W). Notably, the calculated results from the two methods exhibit a close correspondence. For the area of high negative wind pressure, the results of the EAM are marginally higher than that of the PFM. For low negative wind pressure regions, the results of PFM are slightly greater than that of EAM. Therefore, it is safe to use the envelope results of the two methods in the calculation of the standard wind load of the enclosure structure, ensuring a comprehensive and conservative consideration of extreme conditions.

4.2. Standard value of wind load

The measurement points exhibit significant positive and negative values of the standard wind load of the conference center at various wind angles and the corresponding results are presented in **Table 3**. It is found that the measuring points and wind direction angles of the roof with pronounced pulsating positive and negative wind pressures are various. For the upper roof surface, at measuring point F20, the maximum pulsating positive wind pressure reaches 3.15 kN/m^2, occurring at a wind direction angle of 0°. The peak pulsating negative wind pressure (-9.69 kN/m^2) is recorded at 270°, accompanied by a wind pressure coefficient of -4.25. For the entire conference center, the maximum pulsating positive wind pressure (4.83 kN/m^2) appears at the measuring point (R29) of the roof ridge curtain wall on the east elevation, where the wind pressure coefficient is 1.86 and the wind direction angle is 60°. Additionally, the maximum pulsating negative wind pressure (-9.69 kN/m^2) is identified at the measuring point (K1) on the upper surface of the upper roof, where the associated wind pressure coefficient is -4.255 and the wind direction angle is 255°.

The distribution of roof wind pressure has been extensively verified through wind tunnel tests and wind pressure measurements, and studies have shown that areas such as the edges, corners, and ridges of the roof generally experience higher wind pressure. These results align with both experimental data and theoretical models, especially when considering factors such as wind direction, roof geometry, and aerodynamic effects. The uneven distribution of metal roof wind pressure is mainly affected by the geometric shape of the roof, wind flow interference, local eddy currents, as well as wind speed and direction.

Table 3
Test results of pulsating wind pressure

Location	Pulsating positive wind pressure				Pulsating negative wind pressure			
	Point ID	Wind pressure coefficient	Wind pressure (kN/m^2)	Wind direction (°)	Point ID	Wind pressure coefficient	Wind pressure (kN/m^2)	Wind direction (°)
The upper roof covers the upper surface	A1	0.94	2.68	300	A11	-2.91	-8.57	30
	B14	1.03	2.90	300	B2	-2.64	-6.10	300
	C4	0.87	2.52	45	C5	-3.02	-7.08	60
	D51	0.70	2.20	315	D33	-2.45	-5.27	315
	E47	0.63	2.06	345	E10	-3.01	-6.48	75
	F20	1.11	3.15	0	F32	-2.72	-5.86	300
	G20	0.34	3.11	345	G36	-3.15	-7.18	30
	H11	0.86	2.57	210	H31	-2.66	-6.08	240
	J1	0.96	2.81	150	J30	-3.03	-6.53	30
	K36	0.68	2.12	45	K1	-4.25	-9.69	270
The lower roof covers the upper surface	M1	0.67	2.07	195	M18	-3.02	-7.06	270
	N9	0.59	1.89	195	N1	-1.88	-4.59	270
	P20	0.55	1.81	45	P40	-4.10	-9.38	240
The lower surface of the roof	AX53	1.10	3.02	30	AX22	-1.88	-4.05	75
	KX2	0.62	1.97	195	KX1	-2.42	-5.78	225
	PX1	0.97	2.75	255	PX38	-1.38	-3.66	75
Belvedere	Z1	1.59	3.61	285	Z5	-4.33	-8.46	45
West elevation ridge curtain wall	Q51	1.40	3.77	285	Q29	-2.52	-6.03	210
	S17	1.20	3.31	285	S14	-1.54	-3.49	30
East elevation ridge curtain wall	R29	1.86	4.83	60	R23	-3.59	-8.37	165
	T22	1.74	4.54	60	T46	-1.98	-4.27	300
South facade curtain wall	U23	1.47	3.83	30	U2	-1.74	-4.18	15
North facade curtain wall	V23	1.01	2.79	225	V2	-1.06	-2.61	210
West side canopy	W5	0.97	2.19	285	W1	-2.58	-3.59	165
East side canopy	Y3	1.85	4.20	60	Y1	-2.91	-3.89	45

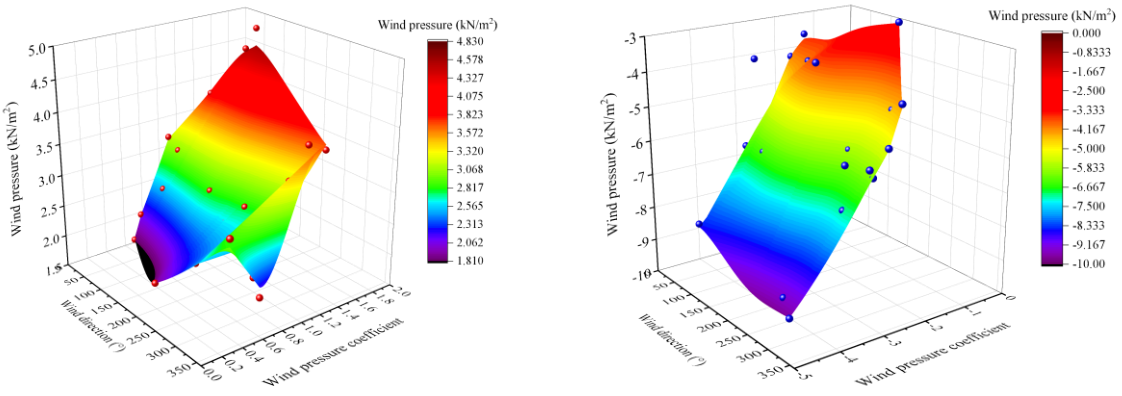

(a) Positive wind pressure (b) Negative wind pressure

Fig. 9 Distribution of pulsating wind pressure

Fig. 9 also shows the relationship between pulsating wind pressure wind direction angle and wind pressure coefficient. It can be found that the variation law of pulsating wind pressure with wind direction angle is not obvious, because different wind direction will cause significant differences in wind loads at different parts. However, the increase of the wind pressure coefficient shows a linear increase trend, which further indicates that the wind pressure coefficient plays a key role in the wind load value of metal roofs.

4.3. Isogram of wind vibration coefficient

As depicted in **Fig. 10,** the wind vibration coefficient of the upper surface of the roof of the conference center is taken as an example. The distribution diagram illustrates the culmination of the body shape coefficient under both pulsating positive and negative wind pressures. It is found that when the wind direction angle is 0°, the isogram distribution of wind vibration coefficient on the roof surface exhibits a relatively scattered pattern **(Fig. 10a)**, and the isogram distribution is positive in most areas, there are notable negative areas only in the southern sector of the conference center, resulting in a comparatively sparse isogram distribution. As shown in **Fig. 10(d)**, when the wind direction angle is 315°, the isogram distribution of the wind vibration coefficient on the upper surface of the roof predominantly manifests two distinct areas. The southern side of the roof mainly shows the cross-distribution of positive and negative wind vibration coefficients, whereas the northern part primarily displays a positive wind vibration coefficient area. This variation is heavily contingent on the specific direction of the wind angle.

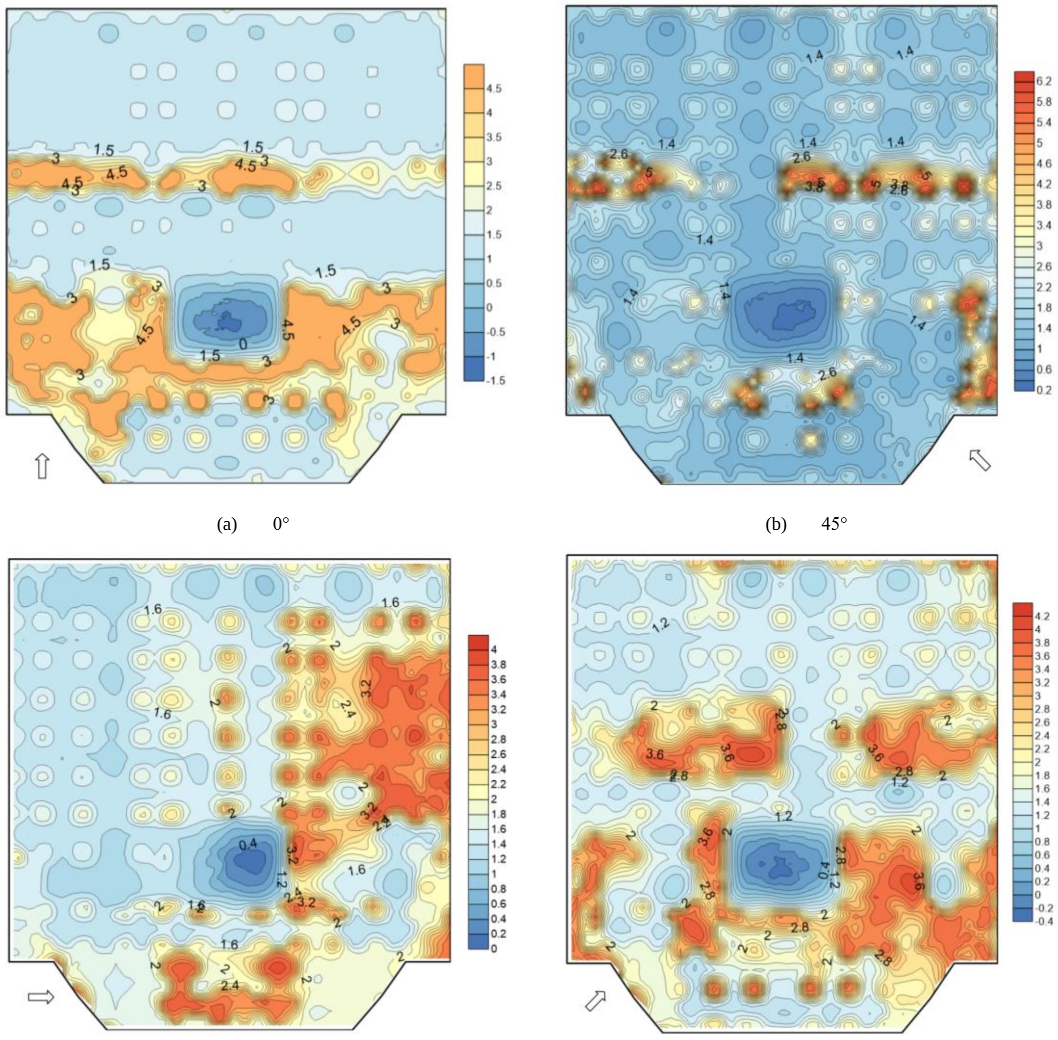

(a) 0° (b) 45°

(c) 270° (d) 315°

Fig. 10 Distribution of wind vibration coefficient

5. Wind vibration calculation and result analysis

5.1. Wind vibration calculation principle

The method employed for analyzing the time history of structural wind vibration responses involves discretizing the structure through the fundamental principles of finite element analysis. The time history of wind load was applied on the corresponding element node and the response of the structure was by directly solving the motion equation in the time domain. While the calculation results obtained through the time domain method align more closely with reality compared to the linear method in the frequency domain, it is typically reserved for critical projects or research verification.

The algorithms utilized in the time domain method can be categorized into direct integration and mode superposition methods. The direct integration method encompasses linear acceleration techniques, *Wilson-θ*, *Runge-Kutta*, and *Newmark-β* methods. In this study, the *Newmark-β* method is specifically employed to compute the time history of the roof structure, tailored to its unique characteristics. The concept of equivalent static wind load is proposed to facilitate engineering applications. When this equivalent load acts on the structure as a static load, the resultant structural response corresponds to the maximum value observed under actual wind load conditions. The equivalent static wind load is commonly expressed as the product of static wind load and wind vibration coefficient (λ). This coefficient accounts for the amplification effect of fluctuating wind loads on structural responses. The load wind vibration coefficient is defined using Eqs. (10).

$$\lambda = \frac{P_e}{\overline{P}} = \frac{\overline{P} + P_d}{\overline{P}} = 1 + \frac{P_d}{\overline{P}} \tag{10a}$$

$$P_d = gm(z)\omega_1^2\varphi(z)\sigma_1 \tag{10b}$$

Where λ is the wind vibration coefficient, P_e is the equivalent static wind load, P Is the static wind load, P_d is the dynamic wind load, g is the peak factor, generally g=2.5, $m(z)$ is the total mass of z height, ω_1 is the circular frequency of the first vibration mode. $\varphi(z)$ is the first-order mode coefficient of the structure at the height of z, and σ_1 is the root mean square of the generalized displacement of the first mode.

In the wind vibration time history analysis of intricate spatial structures, several challenges arise when applying the defined load wind vibration coefficient as per the code. i) Due to the presence of multiple vibration modes in complex spatial structures, the selection of the appropriate vibration modes is difficult. ii) The acceleration response of each joint can be obtained in the FE analysis of wind vibration. If the acceleration response is used to calculate the wind vibration coefficient, only the maximum inertia force can be obtained without considering the wind vibration background component. The wind vibration coefficient calculation method stipulated essentially includes the additional force arising from the wind vibration background component and the resonance component in the code. iii) The specification for the wind vibration coefficient typically employs a single mass block to account for the vibration of the vibrating body. Consequently, in cases where the force transmission path of the vibrating body in the direction of wind pressure is unclear, substituting the mass block becomes impractical, rendering the determination of the load wind vibration coefficient unattainable.

The displacement wind vibration coefficient is a type of effective wind vibration coefficient, determined by the ratio of the maximum displacement to the average displacement response of a structure. The displacement wind vibration coefficient has been applied successfully in high-rise buildings and roof structures dominated by first-order modes. The displacement response includes the background and resonance component of wind vibration. The maximum displacement (U_{max}) generated by dynamic wind load can be calculated using Eq. (11).

$$U_{\max} = \overline{U} + g\sigma_u \tag{11}$$

Where the mean displacement is denoted by, and σ_u is the mean square of displacement. The maximum displacement vector generated by the dynamic wind load is assumed to be equal to the displacement vector generated by the equivalent static load, the displacement wind vibration coefficient can be derived from the definition of the specification. The static equilibrium formulation of the structure under the action of average wind load and equivalent static wind load is shown in Eqs. (12).

$$[K]\{\overline{U}\} = [\overline{P}] \tag{12a}$$

$$[K]\{\overline{U} + g\sigma_u\} = [P_e] \tag{12b}$$

Then the displacement wind vibration coefficient is shown in Eqs. (13).

$$\{\beta\} = \frac{[K]\{\overline{U} + g\sigma_u\}}{[K]\{\overline{U}\}} \tag{13a}$$

$$\beta_i = \frac{P_{ei}}{\overline{P}_i} = \frac{\sum\limits_{j=m,\, j\neq i}^{n} k_{ij}(\overline{U}_j + g\sigma_{uj}) + k_{ii}(\overline{U}_i + g\sigma_{ui})}{\sum\limits_{j=m,\, j\neq i}^{n} k_{ij}\overline{U}_j + k_{ii}\overline{U}_i} \tag{13b}$$

Where j is the adjacent joint i, and k_{ii} and k_{ij} are diagonal and non-diagonal elements of row i of the total rigid matrix. If the following two proportional parameters α_1 and α are introduced, the displacement wind vibration coefficient of joint i can be expressed as Eq. (14a).

$$\beta_i = \frac{\alpha_1 + 1}{\alpha_2 + 1} \cdot \frac{\overline{U}_i + g\sigma_{ui}}{\overline{U}_i} \tag{14a}$$

$$\alpha_1 = \frac{\sum\limits_{j=m,\, j\neq i}^{n} k_{ij}(\overline{U}_j + g\sigma_{uj})}{(\overline{U}_i + g\sigma_{ui})k_{ii}} \tag{14b}$$

$$\alpha_2 = \frac{\sum\limits_{j=m,\, j\neq i}^{n} k_{ij}\overline{U}_j}{\overline{U}_i k_{ii}} \tag{14c}$$

Notably, when the average displacement of each joint is large enough compared to the mean square, or the mean square of each joint is in the same proportion to the average. At this time, the wind vibration coefficient obtained from the definition of load wind vibration coefficient is consistent with the displacement wind vibration coefficient, as shown in Eq. (15).

$$\beta_i = \frac{\overline{U}_i + g\sigma_{ui}}{\overline{U}_i} \tag{15}$$

The application conditions of the displacement wind vibration coefficient are that the mean displacement is large enough relative to the mean square, or the basic configuration of the displacement dynamic and the static response have high similarity. Consequently, this method proves effective for structures predominantly vibrating in the first-order mode but is deemed unsuitable for large-span spatial structures with multi-order modes. To address this, a novel approach combining the Load Response Correlation (LRC) method and the Inertial Wind Load method is proposed to account for the equivalent static wind load on structures. Because the equivalent wind load of background response calculated by the load-response correlation method can obtain different equivalent wind load values for each response of each member, it is difficult to apply this method in large-span roofing structures.

According to the engineering practice, this paper puts forward a simplified calculation method for load wind vibration coefficient, which has obtained favorable outcomes in practical applications. The mean square of acceleration obtained from FE analysis was used to calculate the maximum inertial force of the structure. Simultaneously, the mean square of fluctuating wind pressure is employed to assess the maximum wind vibration force on the structure. The load wind vibration coefficient can be simplified using Eq. (16).

$$\lambda_i = 1 + \frac{g\sqrt{(m_i\sigma_i)^2 + (C_{pi}W_rA_i)^2}}{\overline{C}_{pi}W_rA_i} \tag{16}$$

Where m_i is the total mass of the vibrating body corresponding to the i joint; the mean square of the acceleration of i joint obtained from the σ_i time-course analysis; $\overline{C}_{pi}$ and C_{pi} are the average wind pressure coefficient and the root mean square wind pressure coefficient, respectively. *Wr* is the reference point wind pressure; A_i is the corresponding area of wind pressure acting on the *i* joint; *g* is the peak factor.

Structural damping must be specified in structural dynamic analysis. In this paper, Rayleigh structural damping is adopted, as shown in Eq. (17). Where *C* is the total damping matrix of the system; *M* is the mass matrix of the structure; *K* is the stiffness matrix of the structure; *α* and *β* are constants in Rayleigh damping.

$$C = \alpha M + \beta K \tag{17}$$

The values of *α* and *β* cannot be directly acquired from the real structure but can be derived from the damping ratio of the structure. ξ_i is the damping ratio relative to the *i*-order mode of the structure. If ω_i is the frequency of the *i*-th mode of the structure, the relationship between ξ_i and *α* and *β* can be expressed using Eq. (18). It is generally believed that the *ξ* is constant in a certain structural natural vibration frequency range, so given the *ξ* and two frequencies within this range, *α* and *β* can be obtained, and the *ξ* of the steel structure is 0.02.

$$\xi_i = \frac{\alpha}{2\omega_i} + \frac{\beta\omega_i}{2} \tag{18}$$

The sampling frequency of pulsating wind pressure measurement in the wind tunnel test is 31.5 Hz, with a sampling interval of 0.0032 s. According to the test wind speed ratio of 1:4.28 and the model scale ratio of 1:220, the test time ratio of 1:51.3 can be obtained, and the actual sampling time interval is 0.164 s. The wind pressure coefficient at each measuring point of the structure can be calculated using Eq. (19).

$$C_{pi}(t) = \frac{P_i(t)}{P_0 - P_\infty} \tag{19}$$

Where C_{pi} represents the wind pressure coefficient at the measuring point *i*, P_i denotes the wind pressure acting at that same point, P_0 and P_∞ refer to the total pressure and static pressure at the reference height during the test, respectively. For the wind tunnel test of the roof structure, the reference point is located at a height of 0.6 m, and considering the model scale of 1:220, the actual height of the reference point is 132 m. Using a basic wind pressure of 0.95 kN/m^2, the wind pressure time history corresponding to the measurement point in the actual building can be calculated by obtaining the C_{pi}(t) time history for each point, as shown in Eq. (20).

$$P_i(t) = C_{pi}(t) \times 1.284 \times (\frac{132}{10})^{0.24} \times 0.95 = C_{pi}(t) \times 2.66(\text{kN/m}) \tag{20}$$

Following the determination of the Finite element (FE) model, the wind load time history data at each measuring point undergoes spatial interpolation to formulate P_i(t) at individual stress joints. The control area (A_i) of each stress joint is calculated according to the coordinate relationship within the FE model. Due to the complexity of the structure, the wind load value of each joint can be decomposed into *x*, *y* and *z* directions, as illustrated in Eqs. (21). Where A_{xi}, A_{yi} and A_{zi} represent the projected areas in the *x*, *y* and *z* directions, respectively.

$$F_{xi}(t) = P_i(t) \times A_{xi} \tag{21a}$$

$$F_{yi}(t) = P_i(t) \times A_{yi} \qquad \text{(21a)}$$

$$F_{zi}(t) = P_i(t) \times A_{zi} \tag{21c}$$

The wind load time history of each joint in *x*, *y* and *z* directions is applied to the FE model of the roof structure to calculate the wind-induced dynamic response. The time domain calculation method employed the *Newmark-β* method. The displacement response time history (U_i) and acceleration response time history (α_i) of each joint can be obtained, and the displacement mean square (σ_{ui}) and acceleration root mean square (σ_{ai}) can be calculated through statistics. The wind load of all joints is accumulated to determine the overall wind load of the roof in the *z* direction, and the overall wind vibration coefficient (β_f) of the roof structure is calculated, as shown in Eq. (22). Where, F and F are the cumulative values of the equivalent and average wind load, respectively.

$$\beta_f = F / \overline{F} \tag{22}$$

5.2. Calculation model

In this calculation, 3D3S and other models established previously were used and imported into ANSYS software through interface files. **Fig. 11** shows the FE model of the conference center, in which the total number of joints is 72951. Notably, 2803 joints and 50,343 rods within the model are directly exposed to the influence of wind loads.

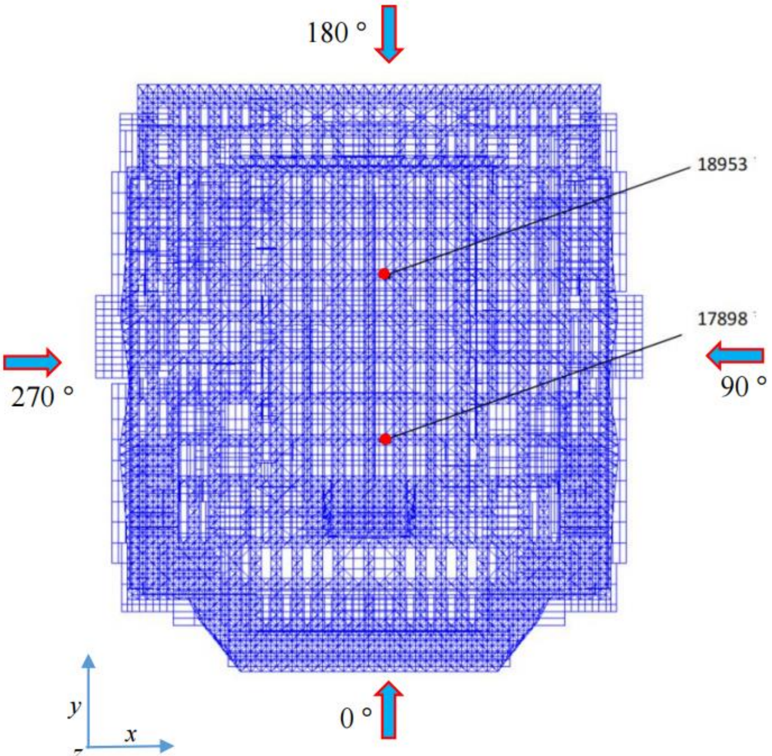

(a) Top view

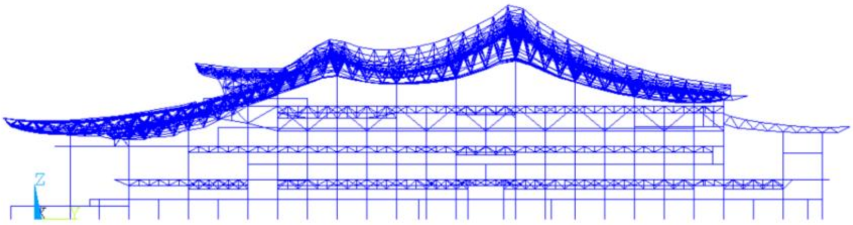

(b) East elevation view

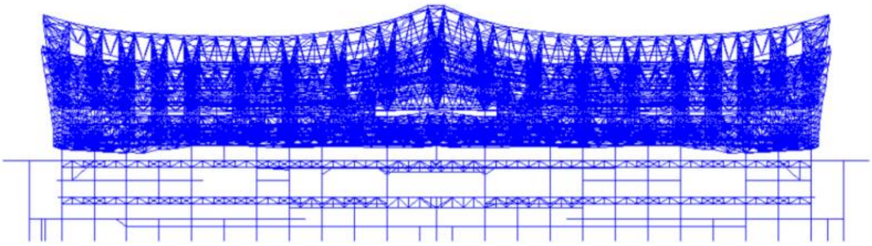

(c) South elevation view

Fig. 11 Finite element model of conference center roofing structure

5.3. Analysis of wind vibration calculation results

The displacement time history of typical joints of the metal roofing structure, namely joints 18953 and 17898 (**Fig. 11**), under 0° wind direction is obtained by calculation, as depicted in **Fig. 12**. It can be found that under this wind direction, the predominant displacement at the joint occurs in the positive *z*-direction (vertical). The displacement in the *x* direction (sideways) and the *y* direction (downwind) is nearly negligible.

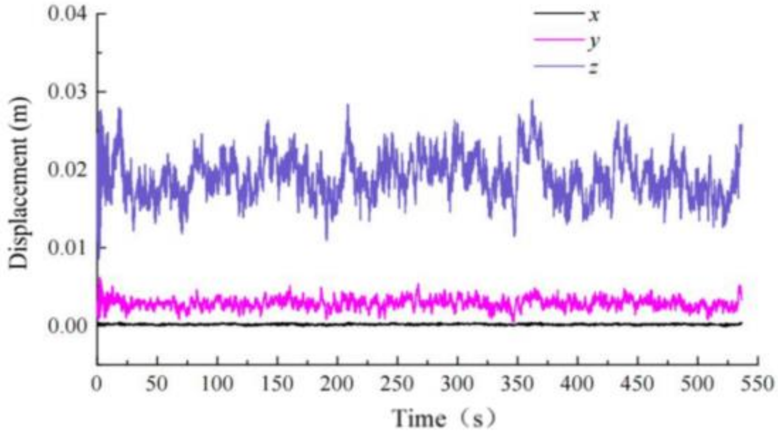

(a) Joint of 18953

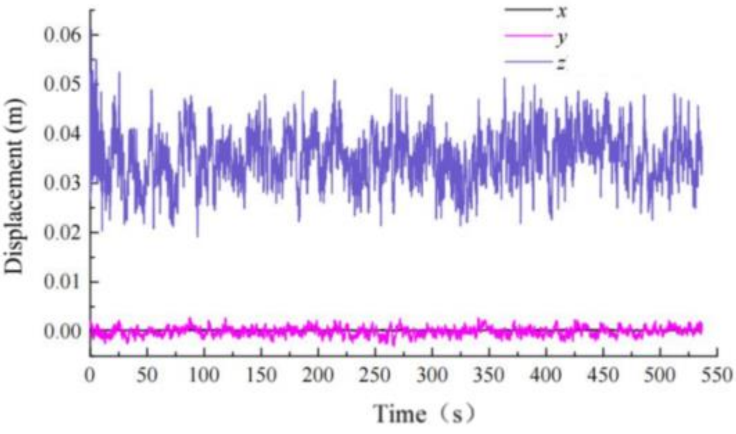

(b) Joint of 17898

Fig. 12 Displacement time history of typical joints at 0° wind direction

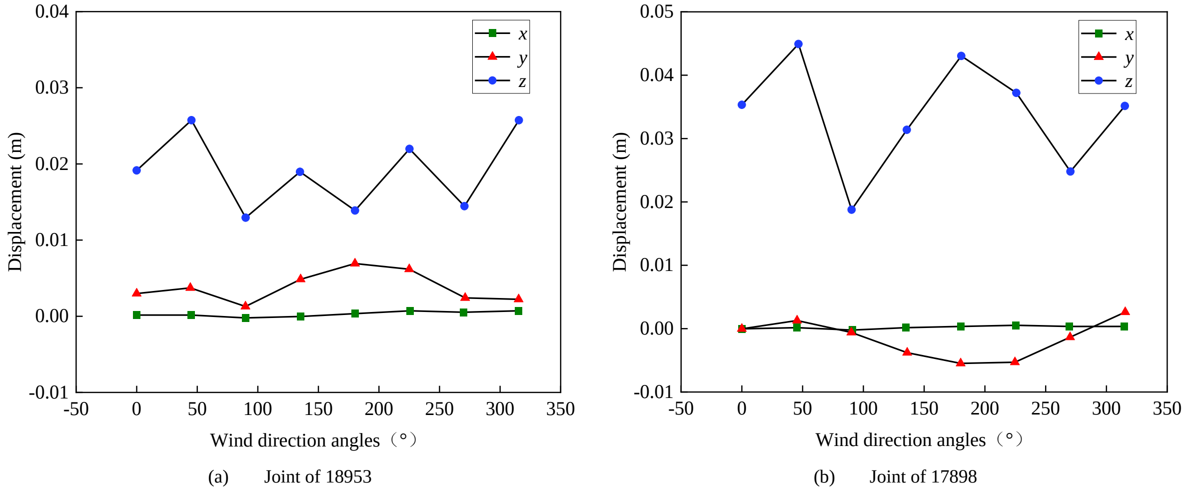

(a) Joint of 18953

(b) Joint of 17898

Fig. 13 The average displacement of typical joints under various wind directions

Taking the joints 18953 and 17898 of the metal roofing structure as typical examples, the average displacements under various wind directions are illustrated in **Fig. 13**. The results indicated that the primary displacement of these joints occurs in the *z*-direction (vertical), while displacements in the *x* and *y* directions are nearly negligible. In the *z*-direction displacement of this joint 18953, all displacements are oriented upward. Notably, the largest displacements are observed at wind angles of 45° and 315°, indicating that the metal roofing structure withstands greater wind loads near the position of this joint.

The forces F_x, F_y and F_z of each joint in the *x*, *y* and *z* directions were calculated, with the wind direction angle defined as depicted in **Fig. 11(a)**, which is consistent with the definition in the FE analysis. The average wind load and equivalent wind load values for each joint at wind angles of 0°, 45°, 90°, 135°, 180°, 225°, 270° and 315° can be directly applied to 3D3S structural design software.

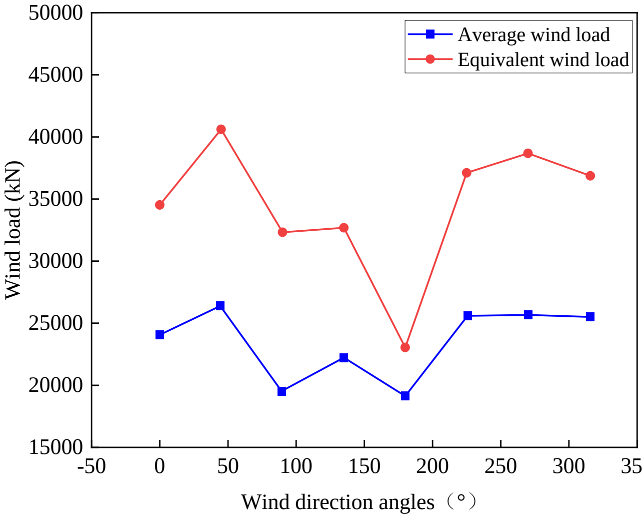

Fig. 14 Wind loads in the *z* direction of the metal roofing

Fig. 14 shows the variation trend of the wind load in the *z*-direction with the different wind direction angles. The average wind load and equivalent wind load for 2803 upper roof joints in the *z*-direction were obtained in the FE calculation. The wind load has taken into account the wind load area, and its unit is kN/m^2. The basic wind pressure utilized in the calculations is 0.95 kN/m^2, which is once in 100 years. **Table 4** presents all the calculated results for the *z*-direction, it can be indicated that the equivalent wind load and the average wind load in the *z*-direction reach the positive peak at a wind direction angle of 45°, and the wind vibration coefficient corresponding to the ultimate wind load is determined to be 1.54.

Table 4
Overall wind loads of conference center roof structure

Wind direction	Equivalent wind load	Average wind load	Vibration
0	34546	24072	1.44
45	40598	26333	1.54
90	32307	19588	1.65
135	32655	22127	1.48
180	23100	19191	1.20
225	37159	25712	1.45
270	38594	25734	1.50
315	36946	25524	1.45

Fig. 15 also presents the average wind load and equivalent wind load values in the *x* and *y* directions for the metal roof panel of the conference center. The wind load acting on the roof structure in the *z*-direction surpasses that in the other two directions. Specifically, the minimum equivalent wind load in the *x* direction is approximately -1200 kN, occurring at a wind direction angle of 90°. The minimum equivalent wind load in the *y* direction is about -17000 kN with a wind direction angle of 180°. The minimum equivalent wind load in the *z* direction is approximately -23100 kN at a wind direction angle of 180°. The maximum equivalent wind load in the *z* direction exceeds 40598 kN and the wind angle is 45°. It is indicated that the ability of the roof to withstand wind load in the *z* direction plays a critical role, which should be considered in the design.

6. Wind damage and strengthening measures of metal roofs

6.1. Discussion on wind damage

Metal roofing systems have been developing continuously with the diversification of roofing applications and the change in structural requirements. Roofing in the service process also appeared to be a variety of engineering problems, as a light discontinuous and large-span metal roof structure wind resistant problem is more prominent. This issue is not confined to coastal areas experiencing the force of strong typhoons; it is prevalent even in inland regions. **Fig. 16** shows the typical failure mode of metal roofs in China [48,49]. The severe weather events have drawn considerable attention due to safety concerns, including incidents of metal roofs being dislodged and collapsing during rainstorms.

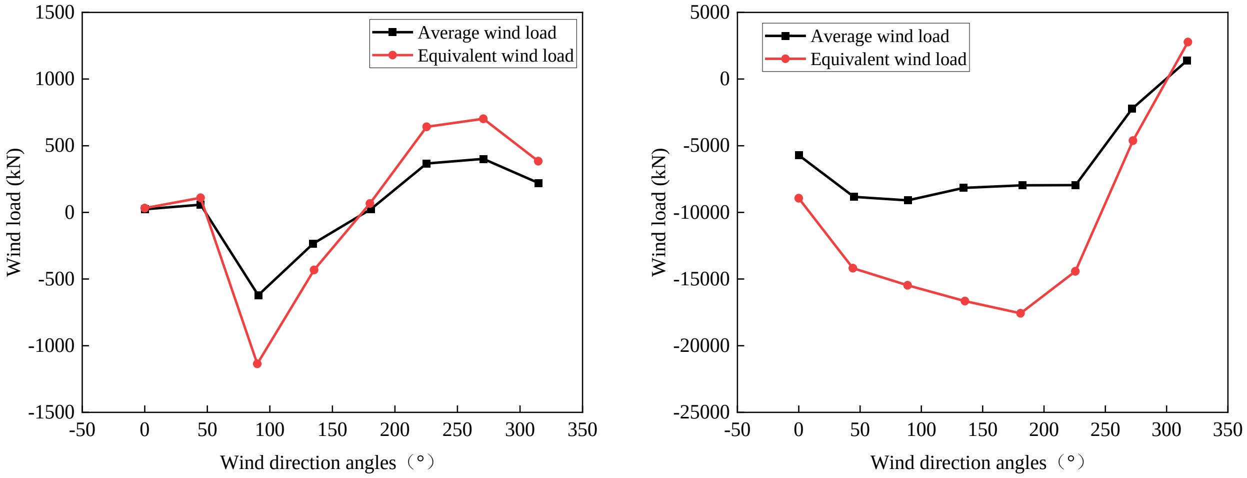

(a) *x* (b) *y*

Fig. 15 Wind load in *x* and *y* directions of the roof structure

(a) Terminal of the capital airport (b) Wuhan Tianhe airport

(c) Suzhou industrial park station (d) Zhanjiang Olympic sports center

Fig. 16 Typical failure modes of metal roofing [48,49]

Table 5
Wind disaster statistics of metal roofing

Time	Project name	Wing load	Failure modes	Roof selection
2010.09	Xiamen Institute of Technology Gymnasium	Super typhoon	The molded steel plate was lifted and the purlin was not damaged	Pressed steel sheet metal roofing
2010.12	Terminal T3 of Capital Airport	Wind speed is 26 m/s，Force 10 gale	Part of the roof metal sheet was torn off by the strong wind	Aluminum magnesium manganese vertical locking metal roofing
2011.11	Terminal T3 of Capital Airport	Wind speed is 24 m/s，Force 9 gale	The roof of Terminal D area was partially torn off by strong winds	
2013.03	Terminal T3 of Capital Airport	Wind speed is 30 m/s，Force 11 gale	The roof in the northeast corner of the international area of the terminal was partially lifted, and the glass cotton of the roof insulation layer was blown off	
2012.08	Suzhou Railway Station Park	Force 10 gale	15 aluminum, magnesium, and manganese plates were thrown open	
2013.08	Wuhan Tianhe Airport T2 terminal	Force 12 gale	The metal plate of the T2 roof was lifted off a corner, and the thermal insulation quilt was blown off by strong winds	
2018.03	Nanchang Changbei Airport Terminal T2	Wind speed is 29.5 m/s，Force 11 gale	The external suspended ceiling material at the T2 overhanging eaves is dropped as a whole, and the roof panel at the arc is large.	

The typical wind damage accidents of metal roofing are listed in **Table 5**. It is found that the damage to the roof system is mainly caused by the following reasons: (i) The design of the roof wind bearing capacity is insufficient; (ii) Insufficient strength in the support and purlin connections; (iii) Failure of the connection between the joint and the bite of the roof plate. The analysis of a large number of roofing accidents reveals that the wind resistance capacity of metal roofing systems primarily depends on the robustness of the supports. Wind disaster investigation shows [50,51] that the damage of standing seam roofing systems is mostly the separation of the roof plate and the fixed support at the lock joint, while the connection between the support and the purlin is still basically intact.

According to the analysis of the causes of the above-mentioned wind damage on the metal roofing, it is found that the phenomenon of wind damage on the roof is mostly caused by the disconnection of the connection between the metal roof plate and the fixed support. When subjected to negative wind pressure, the roof plate initially exhibits an upward arch deformation, as illustrated in **Fig. 17**. In instances of excessive wind suction, this can result in the detachment of the roof plate from the support, leading to damage or severance of the support and the connection with the roofing purlin.

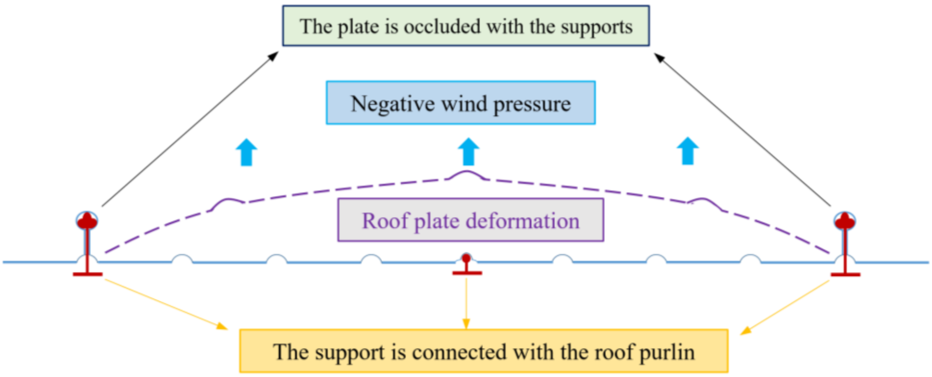

Fig. 17 The wind load transfer way of standing seam metal roofing plate

The examination of the wind resistance performance of metal roofing mainly includes the following key aspects. i) The main load of metal roof under wind load is divided into gas pressure, friction force, and suction force. The gas pressure mainly acts on the roof, the friction operates primarily on the contact surface between the roof and the wind load, and the suction predominantly affects the bottom plate of the roofing. When the wind speed is higher, the pressure and suction on the roof intensify, whereas friction remains relatively constant. Therefore, metal roofing primarily experiences a complex stress state of bending-compression and bending-torsion under a strong wind environment. ii) Various instabilities may manifest in metal roofs when exposed to intense wind conditions, encompassing local buckling, global buckling, and local shear failure. Notably, global buckling stands out as the most prevalent form of instability in such scenarios. iii) The wind resistance performance of metal roofing is affected by many factors, including roof form, material selection, structural design, connection and support system, and the overall roofing load.

6.2. Reinforcement measures of wind resistance

6.2.1. Wind resistance design principles

Under the action of wind loads, the structural surface will form negative wind pressure or trigger structural resonance, which will cause various metal roof damage phenomena. **Fig. 18** illustrates the typical wind resistance mechanism of metal roofing subjected to wind loads. The wind resistance design principles of metal roofing mainly include the following aspects.

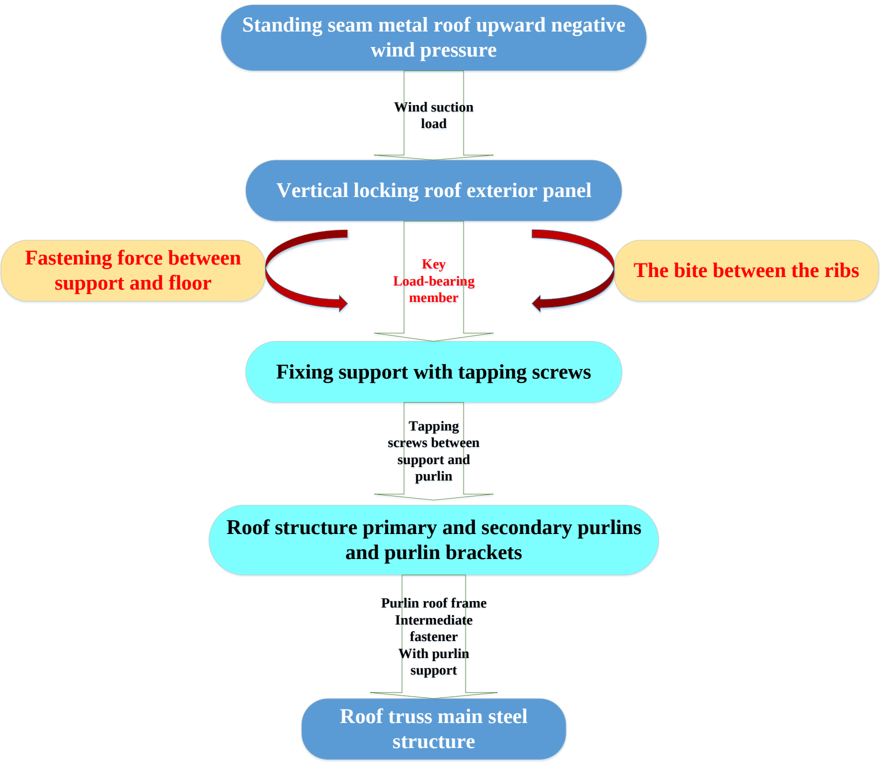

Fig. 18 Typical metal roofing wind resistance mechanism

i) Decreasing the roof load is the pivotal factor in improving the wind resistance of metal roofs. The main measures include optimizing the roof configuration, minimizing the roof weight, lowering roof height, and rationally implementing the roof drainage system.

ii) The improvement of wind resistance of metal roofing is inseparable from the strength and stability of the connection and support system. Specific measures include enhancing the connectivity of the connector, opting for the appropriate connection methods, and enhancing the support strength.

iii) It is very important to choose the appropriate material and construction to improve the wind resistance of metal roofs. Specific measures include the selection of metal materials with good quality and high performance and the design of reasonable support structures.

6.2.2. Windproof design and construction

The standing seam metal roof has also encountered wind-induced challenges in various settings such as airport terminals, large exhibition centers, and sports stadiums. For the prevailing standing seam metal roofing system, several researchers have proposed measures to improve and optimize wind resistance. It is appropriate to ensure key areas and take into account the general area; The strength of the roof plate and the actual strength of the biting part of the fixed support should be determined by the tests. Addressing engineering failure cases, checking calculations and the "short-plate effect" to enhance the strength of the occluding part of the metal roofing plate and the fixed support, as shown in Eq. (23) [52]. The extent of reinforcement between different areas of the roof slab and the occlusal parts of the fixed supports can be established by the experimental tests.

$$F = \min\{F_1, F_2, F_3, F_4\} \tag{23}$$

Where F is the bearing capacity of the weakest part of the roof system; F_1 is the ultimate strength of the lock joint at the support; F_2 is the ultimate bearing capacity of the lock joint without support. F_3 is the ultimate bearing capacity of the fixed support; F_4 is the ultimate bearing capacity of the connecting fasteners.

6.3. Wind resistance measures of this project

The wind tunnel tests are conducted by combining the basic wind pressure once in 100 years with the intricate roofing shape, obtaining the most unfavorable positive and negative wind pressure at each measuring joint in all wind direction angles. The distribution of wind pressure is analyzed, and the locations and areas of the edge region, corner region, and large area are divided. Calculations are performed for the main and secondary purlin sections, spacing, fastener connections, panels, fixtures, eaves, and ridges of each partition. Finally, a solid model is made based on detailed drawings, and dynamic wind resistance tests are carried out.

6.3.1. Structure design and material selection

Metal roofing is susceptible to wind damage in typhoon-prone areas, therefore, selecting high-strength metal roofing materials becomes imperative to ensure stability and load-bearing capacity during strong winds. Currently, the metal roofing plates mainly include: pressed steel plate, titanium zinc plate, aluminum magnesium manganese alloy, and copper plate. For the metal roofing project of XIEC, an aluminum-plated zinc steel plate is selected as the main external maintenance system for the roofing panel. Compared with other materials, aluminum-plated zinc roofing panels have unique advantages, as delineated in **Table 6**.

It is crucial to fully consider factors such as wind pressure, wind load, and wind resistance in the structural design of metal roofing. This project primarily adopted the double-layer metal roofing system, with the detailed structural layer presented in **Fig. 19**. There are reliable connections between the layers to ensure roofing safety under the wind load. To reinforce the connection between the metal roofing and its supports, fasteners, and connectors are strategically positioned on the supporting structure. The metal roofing panels are first connected to the lower fixed supports by bite lock, which in turn are connected between the tapping screws and purlins. Various joints in the roofing structure, including roof standard joints, main and secondary purlins, connection joints, ridge joints, drainage gutter joints, and fall prevention system joints, play a pivotal role. The design quality of these joints significantly contributes to determining the overall wind resistance of the roofing structure.

Table 6
Comparison of roofing panel materials

Roof panel type	Advantage	Limitation
Stainless steel plate roofing	It has excellent corrosion resistance, high strength, long service life, and unique architectural beauty.	Stainless steel plate prices are higher, so only important public construction will be used.
Aluminum magnesium manganese alloy plate	Form a dense oxide film, good anti-corrosion; Lightweight, strong plastic deformation ability, easy to bend molding.	The coefficient of thermal expansion is very high, so the roof plate must leave deformation space for the plate expansion, which also indirectly leads to the overall stiffness of the roof being low, and the wind resistance lacking.
Titanium zinc sheet roofing sheet	Natural passivation layer, no pollution; Corrosion resistance; With self-cleaning function, save operating costs; Good flexibility, convenient processing.	Titanium zinc plate is expensive, about 10-15 times that of aluminum magnesium manganese alloy roof plate. Although titanium zinc plate is favored by roof designers, it is not widely used in public buildings.
Copper roofing panel	With natural copper oxide passivation film, good protection ability; Good plasticity, easy to process; Flame retardant, and recycling advantages.	Due to the relatively high price of copper sheets, copper sheet roofing is rarely used in large public buildings in China.
Aluminized zinc roofing panel	Good flexibility and ductility; Strong corrosion resistance and heat resistance, and high thermal reflectivity, so it is widely used in China.	Once the aluminized zinc plate is cut, it will rust quickly when the cut edge is unprotected. Once cut, an anti-rust paint or zinc-rich paint is applied to protect the edge, which can extend the service life of the sheet.

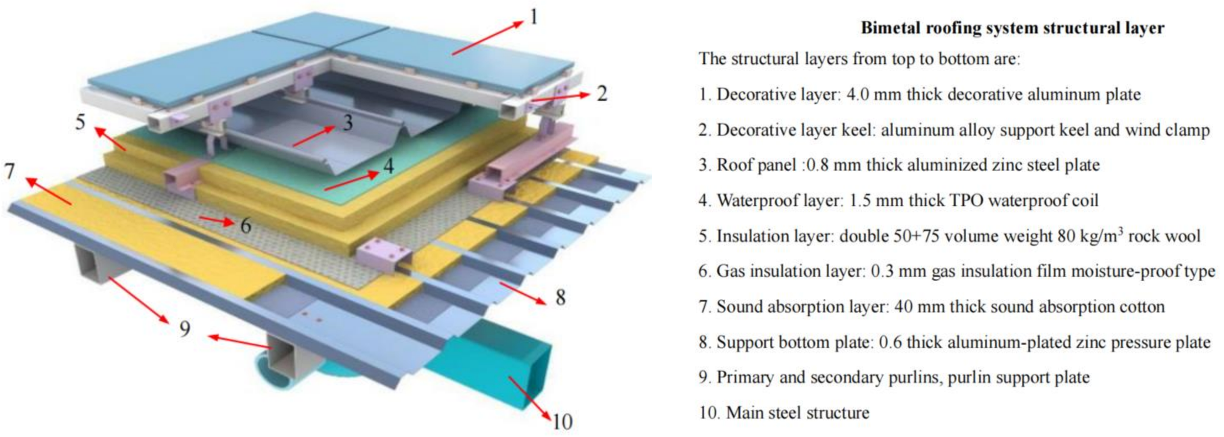

Bimetal roofing system structural layer

The structural layers from top to bottom are:

1. Decorative layer: 4.0 mm thick decorative aluminum plate
2. Decorative layer keel: aluminum alloy support keel and wind clamp
3. Roof panel :0.8 mm thick aluminized zinc steel plate
4. Waterproof layer: 1.5 mm thick TPO waterproof coil
5. Insulation layer: double 50+75 volume weight 80 kg/m^3 rock wool
6. Gas insulation layer: 0.3 mm gas insulation film moisture-proof type
7. Sound absorption layer: 40 mm thick sound absorption cotton
8. Support bottom plate: 0.6 thick aluminum-plated zinc pressure plate
9. Primary and secondary purlins, purlin support plate
10. Main steel structure

Fig. 19 Structural layers of bimetal roofing system

The wind resistance performance of metal roofs is an important measure to ensure the safety of roofing structures. The stainless steel continuous welding roof is preferred in areas with high wind-resistant requirements, and aluminum alloy standing seam metal roofing is avoided as far as possible. Structural strengthening measures should be taken in the special areas of the roof, such as the cornice and arch. This project has taken some strengthening measures to effectively address the aforementioned concerns. The laying of metal plates should pay attention to the perennial wind direction, and the lapping of plate ribs should be opposite to the wind direction. Securing the fixed support within the vulnerable wind-protected zone by aligning it along the longitudinal direction of the board. When installing galvanized steel fixed supports in the encrypted area, incorporate a hot-dip galvanized steel support to bolster the wind resistance of the eaves section. In the context of the aluminum-plated zinc standing seam metal roofing system, employ galvanized steel fixed supports for fixation. Subsequently, affix the roofing plate onto the support, and use an electric edge-locking machine to secure the plate rib onto the fixed seat. This method avoids penetrating the plate surface, averting stress concentration, and contributing to superior wind resistance.

6.3.2. Construction and transportation phase

This project encountered several challenges in the construction process, as shown in **Fig. 20**. An error in the spacing or angle of fixed seat installation, coupled with difficulties in operating the edge-locking machine on corner parts, led to incomplete roofing panels. These areas represent the most vulnerable zones against negative wind pressure, and once the wind is inserted, it is likely to be damaged by the wind. The structure is prone to overturning or being dislodged by wind load originating from the cornice. The substantial wind pressure at the eaves poses a risk during the installation of galvanized steel fixing seats. Insufficient strength in the screws may weaken the pulling force of the fixing seat, resulting in failure.

The structure configuration of the standing seam metal roof is inherently intricate, with the construction quality posing a substantial challenge. The overall quality of the construction process plays a pivotal role in determining the wind resistance and waterproof capacities of the roofing. During the construction phase of a metal roof, it is necessary to strictly control the angle and installation direction of its wind surface to avoid the phenomenon of opening and warping under the action of strong winds. The key technical processes integral to the construction phase encompass the following aspects.

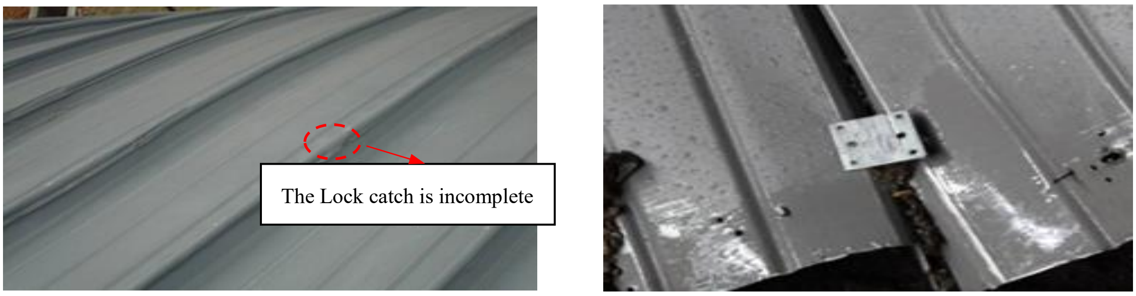

(a) The overlock is incomplete

(b) The strength of the fixed seat is weakness

Fig. 20 The problems in the construction of roofing panels

6.3.2.1. Roofing plate processing and transportation

The transportation of metal roofing panels can be combined with ramps and tower cranes. The finished roof panels were transported to the middle of the roof along the upper ramp and installed from the midpoint towards both sides. Short roof plates, having undergone ground pressing and forming, are transferred to the roof using a welding square tube flatbed truck on the ground. The longer roof plates need to be transferred by two simultaneously to prevent excessive deflection and bending damage. After the roofing plate is transported to the roof, it is horizontally lifted to the installation site, as shown in **Fig. 21 (b)**.

(1) Due to the manual handling involved in the transportation of roof panels, considering that the roof panel is prone to deformation during the handling process. Therefore, the slope of the ramp for the upper board can't be too large, and it is controlled below 30 °. To further mitigate risks, roofing panels are strategically handled at intervals of 10 meters. Upon reaching the roof, the panels are uniformly arranged in the predetermined stacking location.

(2) Rigorous and effective protective measures are imperative throughout the production and vertical/horizontal transportation of the panels. This is crucial to guarantee the integrity of the roof panels, with any damaged panels strictly prohibited from being used in the project. The vertical transportation method involves a ropeway system and bench lifting, a combination chosen to safeguard the roofing panels from potential damage.

(3) Post-installation, the finished roofing panel must be protected. Walking on or subjecting it to impact from hard objects is strictly forbidden. The installed roof is not allowed to place heavy objects, especially metal materials.

(a) Roofing plate bending and arc processing

(b) Roofing panel transport in place

Fig. 21 Schematic diagram of metal roofing plate processing and installation

6.3.2.2. Construction quality of purlin and support

The installation process for hot-dip galvanized steel purlins must adhere rigorously to the prevailing installation specifications for steel structures, ensuring that the welds of the purlins meet the Grade II standard. During the installation of purlins, utmost attention must be paid to prevent any secondary scratching of the hot-dip galvanized surface. Additionally, any purlins that incur scratches during installation must be meticulously addressed to prevent the installation of damaged purlins on the roof. Purlins are installed by the tower crane and car crane through a hook and multiple lifting, as shown in **Fig. 22 (a)**.

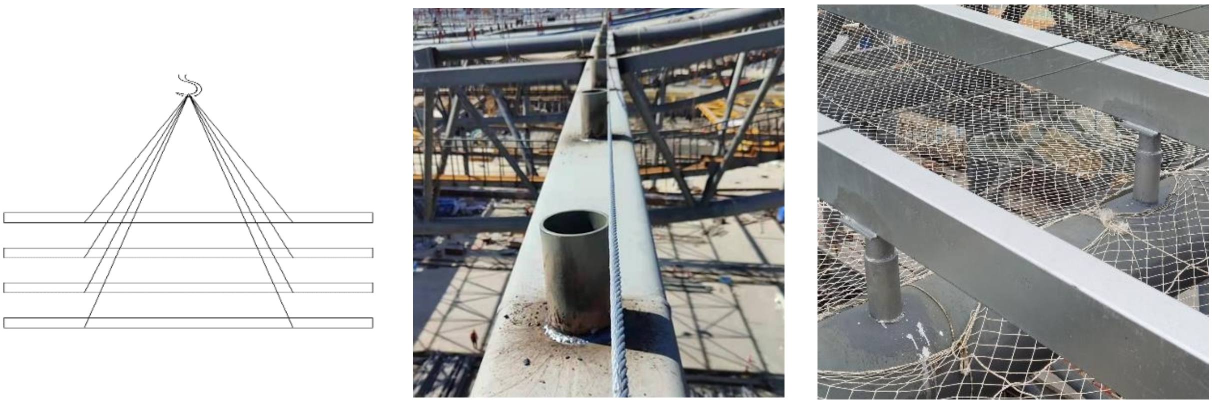

(a) Purlin hoisting (b) Support installation (c) Purlin installation

Fig. 22 Purlin and support installation diagram

Due to the upper purlin support is a second purlin, the second purlin is first used to pop out the control line on the main purlin along the slope of the roof according to the distance of the purlin. Subsequently, the support locations for the second purlin are marked on the main purlin using the positioning line. A hot-dip galvanized purlin steel plate support is welded onto the designated position. The primary purlin reinforcement zone is predominantly situated near the ridge and overhanging eaves, areas subjected to greater negative wind pressure. The primary purlins are distributed in the middle of the roof, which is bolted on the primary purlin bracket. The primary purlin in other positions is welded at one end and the other end is bolted, and the local area is welded at both ends. The overall arrangement direction of the main purlin is perpendicular to the direction of the steel structure truss, and the secondary purlin is filled during the arrangement. Whereas, the overall arrangement direction of the primary purlin in other positions is parallel.

6.3.2.3 Installation of pressed steel bottom plate

The bottom plate for the roofing is made of aluminum-zinc-plated perforated pressed steel, with a thickness of 0.6 mm and a galvanized surface. The yield strength is more than 250 MPa, tensile strength exceeds 330 MPa. Positioned above both the primary and secondary purlins, this steel bottom plate is affixed to the primary purlin using self-tapping nails at the installation trough. The orientation of the bottom plate is perpendicular to the direction of the secondary purlin, as illustrated in **Fig. 23**. The length of the bottom plate is determined by the spacing of the adjacent purlins, and the connection between the bottom plate is the lap joints fixed onto the primary purlin with special steel nail connections.

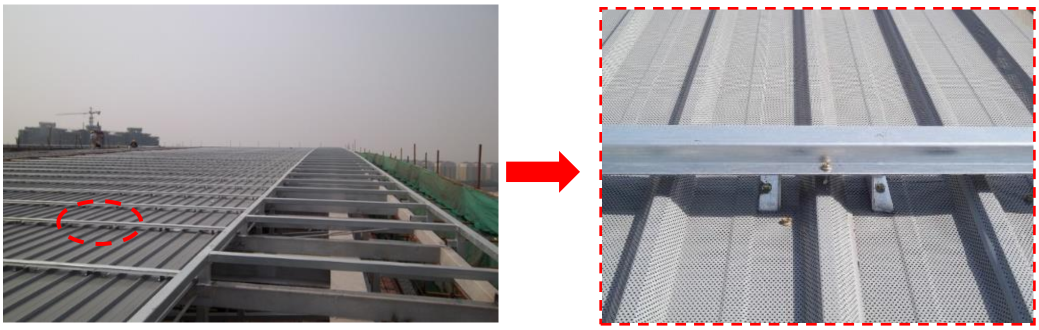

Fig. 23 Installation diagram of the base plate of metal roofing

The installation of the bottom plate starts from the edge line of the gable and spreads from one side to the other, the frame at the cornice of the gable is used as the reference line to determine the installation axis of the bottom plate. The installation of the roof bottom plate directly affects the performance of the whole roof. Therefore, it is imperative to conduct a thorough reassessment of the steel structure purlins and the elevations of key components already installed on the construction surface before installing the roofing plate. The bottom plate of the project is located under the secondary purlin, the additional primary purlin is placed on, which is reverse lifted construction through the hanging basket.

6.3.2.4. Mounting quality of the fixed support

The fixed support for aluminized zinc roof plates plays a pivotal role in transferring the wind load from the roof to the secondary purlin. The galvanized steel fixing base comprises both a galvanized steel base and galvanized steel stranding pieces, these components are integrated using M8 self-tapping and self-drilling screws to form a cohesive support structure. Due to the thermal expansion and contraction processes, the roof plate is allowed to freely slip, thus mitigating the risk of plate fracture resulting from improper installation. During the installation of the galvanized steel fixed base, it is imperative to first apply butyl tape and a modified asphalt gasket beneath the support. The installation of the support adopts two symmetrical self-tapping nails. A self-tapping screw is initially driven, followed by a corrective adjustment of the support to rectify any deviation. After the correction, insert the second screw and fix it, tighten the screws properly to avoid heavy or floating nails. **Table 7** lists the installation requirements for the support.

Table 7
Galvanized steel fixed base installation dimension deviation requirements

Description	Permissible error
Transverse angle	Deviation from roofing reference line <1°
longitudinal angel	Deviation from roofing reference line <1°
Longitudinal fixed seat height deviation	Less than 1/200 fixed seat spacing
Lateral fixed seat height deviation	≤3 mm
Longitudinal axis deviation	≤2 mm

(a) Drilling at fixed points (b) Roof panel locking

Fig. 24 Roofing panel fixing and locking edge process

6.3.2.5. The occlusal quality of the standing seam roofing plate

When securing the edges, the plates are arranged in the direction of the small lock edge line, with the larger lock edge overlapping the smaller one. Generally, the plate is installed from one end of the roof to the other end, as illustrated in **Fig. 24 (b)**. However, in certain unique circumstances, adjustments to the laying order of the plates may be necessary. A different panel installation sequence may be required when the roof pitch is perpendicular to the panel orientation.

After adjusting the position of the panel, install the foam seal under the end panel before locking the edge. It is essential that the side after locking remains uniformly continuous and smooth, devoid of any distortion or cracks. As the locking machine advances, particular attention must be given to ensuring that the lap edge joint within the 1-meter range at the front is tightly compressed. The crux of stitching quality lies in the forceful and tight joining of the overlapping edge during the stitching process.

6.3.2.6. Construction quality of key parts

An excessive error in the installation of the fixed seat, or difficulties in accessing corner parts where the locking machine cannot easily operate, can result in incomplete locking of the roof panel. These vulnerable sections are susceptible to negative wind pressure, leading to stress concentration when wind penetrates the roofing panel. Consequently, there is a heightened risk of the roofing panel being lifted during strong winds. To address this during roof construction, emphasis must be placed on enhancing wind resistance through the implementation of robust anti-typhoon emergency plans and temporary measures, including closing the side of the completed area in time, setting up three wind clips and wind rope in the eaves, trenches and so on.

To enhance the wind resistance of standing seam metal roofs, current reinforcement techniques mainly focus on the following aspects: Firstly, optimizing the joint between the roofing plate and support by utilizing locking angles with improved biting efficacy, with existing angles reaching up to 540°, thereby advancing wind resistance. Additionally, increasing the edge height is a widely employed method to improve wind resistance, which can increase the strength and stability of the edge. Augmenting the number of locking edges is another effective strategy, particularly for roofs with standing seam metal roofing. This approach enhances connection points between the metal roof and support structure, thereby boosting overall stability. The supporting structure at the locking edge is the key part of the wind resistance of metal roofing. By strengthening the supporting structure at the lock edge, the stability and strength of the lock edge can be enhanced. For example, the installation of transverse and longitudinal stiffeners at the locking edge can enhance the stability of the support structure. The use of high-strength bolts and reinforcing materials at the locking edge can increase the connection strength and stability of the locking edge, improving the wind resistance of the metal roof.

In the wind tunnel test of metal roofing, the findings of this study also have certain guiding significance for the development of design specifications and engineering practices, which are mainly reflected in the following aspects: Firstly, wind tunnel experiments can provide accurate wind pressure distribution and dynamic response data, which is crucial for evaluating the wind resistance performance of metal roofing under extreme weather conditions. These data can be used to revise existing design codes, ensuring they more closely align with actual wind loads and structural responses. Secondly, the experimental results contribute to optimizing the detailed design of the roof structure, such as strengthening the connecting parts of the roof panel, improving the drainage system, or adjusting the roof shape, to improve the stability and safety of the metal roofing structures. Finally, through comparison with theoretical models and practical engineering cases, the research results can provide a practical basis for the guidelines to ensure that the wind load design is more realistic and targeted.

7. Conclusions

In the current environment of frequent climate change and natural disasters, it is an important issue to improve the safety of large public buildings. Based on the metal roofing project of XIEC, this paper completed the wind tunnel test analyzed the experimental results, and obtained the standard wind load of the conference center envelope structure, the overall wind load of the roofing structure, and the contour line distribution results of the roofing systems under each wind direction angle under the action of maximum wind pressure. The analysis delved into the causes of wind-induced damage to metal roofs and explores common reinforcement methodologies. The following main conclusions can be drawn:

- A wind tunnel test platform was built to simulate the wind load conditions of large metal roofs under different wind speeds, which can simulate the airflow state under different wind speeds and the stress situation of metal roofs. For this wind tunnel test, the geomorphic index α=0.12, the physical height of the wind speed reference point H=132 m, and the basic wind pressure w_0 =0.95 kN/m^2 once in 100 years, the reference wind pressure can be obtained by calculation.
- The structure of the convention and exhibition center is complex, and the space shape is novel. Select typical joint 18953 for analysis, it is found that: i) the displacement of this joint is mainly in the z-direction, and the displacement in the x and y directions is almost zero; ii) In the z-direction displacement of this joint, all displacements are upward, and the displacements at 45° and 315° wind angles are the largest, indicating that the roofing structure under these two wind angles experiences greater wind suction near the position of this joint.
- Peak factor method and extreme value analysis were respectively used to calculate the standard wind load value of the roofing structure. In general, the results of the two methods are close to each other, and the extreme value analysis method can better predict the extreme value of negative wind pressure in the non-Gaussian region of wind pressure distribution. In this paper, the envelope of peak factor method and extreme value analysis method were used to give the standard value of the design wind load of the roofing structure.
- The average wind load and equivalent wind load of 2803 roofing upper joints in the z direction were obtained through FE calculation. It is found that the equivalent wind load and the average wind load in the z direction reach the positive maximum at 45° and 270°, and the overall wind vibration coefficient corresponding to the ultimate wind load is 1.65.
- The stress characteristics and failure modes of metal roofs in a strong wind environment were summarized, and the factors affecting the wind resistance of metal roofing were analyzed. Taking this project as an example, the reinforcement measures for the wind resistance design of metal roofing were proposed, including reducing the roof load, enhancing the wind connection and locking height, and reasonable selection of materials and structures. The possible measures to further improve the wind resistance performance of metal roofs were discussed.

The research on wind resistance performance of metal roofs has promoted the updating of roof structure design and wind protection standards to a certain extent, there are still some problems in the existing research, such as single experimental conditions and insufficient consideration factors. Therefore, future research should pay more attention to the comprehensive consideration of the interaction between wind load and roof system, strengthen the wind resistance performance test under multiple scenarios and conditions, and improve the accuracy and practicability of wind resistance performance evaluation through field data feedback and model calibration.

Acknowledgements

The authors gratefully acknowledge the financial support provided by China Construction Fourth Engineering Division Corp., LTD, Xiamen 361000, China. Key Laboratory of New Technology for Construction of Cities in Mountain Area (Chongqing University) and Xiamen International Expo Center metal roofing innovation technology research team for the work reported in this paper.

References

[1] Lu Q.R, Li M.C, Zhang M.X, Min Q.L, Zhang Y.J, Liu X.D. Wind-resistance performance investigation of 360◦ vertical seam-locked roof system reinforced by sliding support and sandwich panel. Journal of Building Engineering, 2022; 45: 103689.

[2] Ou T, Wang D.Y, Xin Z.Y, Tan J, Wu C.Q, Guo Q.W, Zhang Y.S. Full-scale tests on the mechanical behaviour of a continuously welded stainless steel roof under wind excitation. Thin-Walled Structures, 2020; 150: 106680.

[3] Estephan J, Feng C.D, Chowdhury A.G, Chavez M, Baskaran A, Moravej M. Characterization of wind-induced pressure on membrane roofs based on full-scale wind tunnel testing. Engineering Structures, 2021; 235:112101.

[4] Ignatowicz R.L, Gierczak J. Increase in wind load during assembly causes collapse of the hall structure. Engineering Failure Analysis, 2020; 113: 104538.

[5] Baheru T, Development of test-based wind-driven rain intrusion model for hurricane-induced building interior and contents damage. FIU Electronic Theses and Dissertations, FIU, 2014.

[6] Baheru T, Chowdhury, A.G. Pinelli J.P. Estimation of wind-driven rain intrusion through building envelope defects and breaches during tropical cyclones. NatHazards Rev, 2014;16: 04014023.

[7] Darwish Y, ElGawady M. Finite element analysis of TPO membrane- retrofitted metal roof system subjected to wind loads. Structures, 2023; 50: 330-346.

[8] Tian M.L, Gao X.X, Zhang A.F, Han L.J, Xiao H.T. Study on the deformation failure mechanism and coupling support technology of soft rock roadways in strong wind oxidation zones. Engineering Failure Analysis, 2024;156: 107840.

[9] Tolera A.B, Estephan J, Chowdhury A.G, Zisis I, Sherman E, Kirby J. Wind loading on commercial roof edge metals: A full-scale experimental study. Journal of Building Engineering, 2023; 75:106910.

[10] Pieper L, Mahendran M. Numerical investigation and design of crest-fixed corrugated steel claddings under static wind uplift loading. Thin-Walled Structures, 2023; 182: 110270.

[11] Pawar S, Jugade H, Mukhopadhyay G. Investigation of corrosion of 55AlZn coated roof sheets in Al smelting plant. Engineering Failure Analysis, 2020;115:104691.

[12] Chen W.S, Hao H, Du H. Failure analysis of corrugated panel subjected to windborne debris impacts. Engineering Failure Analysis, 2014; 4: 229-249.

[13] Kopp G.A, Bank D. Use of the wind tunnel test method for obtaining design wind loads on roof-mounted solar arrays. Journal of Structural Engineering, 2012; 139: 284-287.

[14] Li R., Chowdhury A.G, Bitsuamlak G, Gurley K.R. Wind effects on roofs with high-profile tiles: experimental study. Journal of Architecture Engineering, 2014.

[15] Hadane A, Redford J.A, Gueguin M, Hafid F, Ghidaglia J.M. CFD wind tunnel investigation for wind loading on angle members in lattice tower structures. Journal of Wind Engineering & Industrial Aerodynamics, 2023; 236:105397.

[16] Wu B, Zhao H, Chen B, Yang Q.S. Comparison of wind-resistant capacities of standing seam roof systems under static uniform pressures and dynamic non-uniform wind pressures. Journal of Wind Engineering & Industrial Aerodynamics, 2023; 241:105552.

[17] Xia Y.C, Kopp G.A, Chen S.F. Failure mechanisms and load paths in a standing seam metal roof under extreme wind loads. Engineering Structures, 2023; 296: 116954.

[18] Baskaran B.A, Lei W. New design procedure for wind uplift resistance of architectural metal roofing systems. Journal of Architectural Engineering, 2006; 168-177.

[19] Schroter R.C. Air pressure testing of sheet metal roofing. NRCA Second International journal of Roofing Technology, 1985; 254-260.

[20] Xu Q.H, Wan T, Liu K. Optimal design of strengthening wind exposure resistance of vertical whipstitch mental roofing board. Engineering Mechanics, 2020;17-26. (in Chinese)

[21] Farquhar S, Kopp G.A, Surry D. Wind tunnel and uniform pressure tests of a standing seam metal roof model. Journal of Structural Engineering, 2005; 131: 650-659.

[22] Min Q.L, Li N, Zhang Y.J, Lu Q.R, Liu X.D. A novel wind resistance sliding support with large sliding displacement and high tensile strength for metal roof system. Engineering Structures, 2021; 243: 112670.

[23] Sinno R.R, Surry D, Fowler S, Ho T.C. Testing of metal roofing systems under simulated realistic wind loads. In: Proc 11th International Conference Wind Engineering, 2003;1065-1072.

[24] Li M, Yin X.Z, Zhang W, Fan F, Zhu Z.Q. Finite element analysis of wind-resistance performance of standing seam roof. Steel Structures, 2017; 72-76. (in Chinese)

[25] Liang Q.S, Yang Q.S, Liu M, Nie S.D, Wang Z, Liu R.L. An efficient method for evaluating the wind resistance performance of high-vertical standing seam metal cladding systems. Thin-Walled Structures, 2024; 205: 112433.

[26] Wang M.M, Ou T, Xin Z.Y, Wang D.Y, Zhang Y.S, Cui L. Experimental study on static temperature field effect on standing seam metal roof system. Structures, 2021; 31: 1-13.

[27] Simiu E, Miyata T. Design of buildings and bridges for wind: a practical guide for ASCE-7 standard users and designers of special structures. New Jersey: John Wiley & Sons, 2006.

[28] Peov A. Dynamic response and life prediction of steel structures under wind loading. Journal of Wind Engineering and Industrial Aerodynamics, 1998; 1057-1065.

[29] Suresh K. Prediction of wind-induced fatigue on claddings of low buildings. Computers and Structures, 2000;31-48.

[30] Myuran K, Mahendran M. New test and design methods for steel roof battens subject to fatigue pull-through failures. Thin-Walled Structures, 2017; 558-571.

[31] Myuran K, Mahendran M. Unified static-fatigue pull-through capacity equations for cold formed steel roof batten. Journal of Constructional Steel Research, 2017;135-148.

[32] Wu T, Sun Y, Cao Z.G, Zhang J. Wind vulnerability analysis of standing seam roof system considering fatigue damage. Thin-Walled Structures, 2023; 184: 110550.

[33] Sun Y, Wu T, Cao Z.G, Wind vulnerability analysis of standing seam roof system with consideration of multistage performance levels. Thin-Walled Structures, 2021;165(1):107942.

[34] Habte F, Mooneghi M.A, Chowdhury A.G. Full-scale testing to evaluate the performance of standing seam metal roofs under simulated wind loading. Engineering Structures, 2015;231-248.

[35] Holmes J.D. Wind Loading of Structures. CRCPress, Oakville, 2015.

[36] Luo Y.F, Xiao B.B, Liu S. Analysis of the load-bearing capacity of thin-walled steel roof panels and connections. Progress in Steel Building Structures, 2006; 1-4.

[37] Wijesooriya K, Mohotti D, Lee C.K, Mendis P. A technical review of computational fluid dynamics (CFD) applications on wind design of tall buildings and structures: Past, present and future. Journal of Building Engineering, 2023; 74:106828.

[38] Gaur N, Raj R. Aerodynamic mitigation by corner modification on square model under wind loads employing CFD and wind tunnel. Ain Shams Engineering Journal, 2022; 13: 101521.

[39] Shan X.F, Luo N, Sun K.Y, Hong T.Z, Lee Y.K, Lu W.Z. Coupling CFD and building energy modelling to optimize the operation of a large open office space for occupant comfort. Sustainable Cities and Society, 2020; 60:102257.

[40] BaskaranB.A, Ksk P. Optimizing the wind uplift resistance of mechanically attached roofing systems. Journal of Architectural Engineering, 2008; 65-75.

[41] Baskaran B.A, Molleti S, Booth R.J. Understanding air barriers in mechanically attached low slope roofing assemblies for wind uplift. Journal of ASTM International, 2006; 1-13.

[42] Azzi Z, Habte F, Vutukuru K.S, Chowdhury A.G, Moravej M. Effects of roof geometric details on aerodynamic performance of standing seam metal roofs. Engineering Structures, 2020; 225:111303.

[43] ASTM E1592. Standard test method for structural performance of sheet metal roof and siding systems by uniform static air pressure difference. West Conshohocken, PA: ASTM International, 2001.

[44] ANSI/FM Approvals 4474. Evaluating the simulated wind uplift resistance of roof assemblies using static positive and/or negative differential pressures. Norwood, MA: American National Standards Institute, 2004.

[45] UL 1897. Standard for uplift tests for roof covering systems. Cames, WA: Underwriters Laboratories, 2004.

[46] JGJ/T 338-2014, Standard for wind tunnel test of buildings and structures. China Architecture & Building Press, Beijing, 2014. (in Chinese)

[47] GB 50009-2012, Load code for the design of building structures. China Architecture & Building Press, Beijing, 2012. (in Chinese)

[48] Guan W.L. Study on wind-resistant capacity of typical metal roof panels. South China University of Technology, 2019. (In Chinese)

[49] Nan N. Research on the wind resistance performance of large-span metal roof and the bearing capacity of new connectors. Lanzhou University of Technology, 2021. (In Chinese).

[50] Mackiewicz M, Krentowski J.R, Knyziak P, Kowalski R. The influence of the fire temperature on the condition of steel roof structure. Engineering Failure Analysis, 2023;146:107080.

[51] Wang M.M, Ou T, Xin Z.Y, Wang D.Y, Zhang Y.S. Mechanical behavior and fatigue failure analysis of standing seam aluminum alloy roof system under temperature effect. Journal of Building Engineering, 2021; 44: 103001.

[52] Wang M.M, Xin Z.Y, Ge L.F, Wang D.Y, Zhang Y.S. Wind load design and test methods for standing seam metal roofing system. Building Structures, 2023; 1-8.